PERGAMON

International Journal of Solids and Structures 38 (2001) 3161–3192

INTERNATIONAL JOURNAL OF SOLIDS and STRUCTURES

www.elsevier.com/locate/ijsolstr

Damage detection of beams using operational deflection shapes

P. Frank Pai *, Leyland G. Young

Department of Mechanical and Aerospace Engineering, E2403D, Engineering Bldg East, University of Missouri-Columbia, Columbia, MO 65211, USA

Received 26 October 1999; in revised form 23 June 2000

Abstract

This work is an in-depth study of a boundary effect detection (BED) method for pinpointing locations of small damages in beams using operational deflection shapes (ODSs) measured by a scanning laser vibrometer. The BED method requires no model or historical data for locating structural damage. It works by decomposing a measured ODS into central and boundary-layer solutions using a sliding-window least-squares curve-fitting technique. For high-order ODSs of an intact beam, boundary-layer solutions are non-zero only at structural boundaries. For a damaged beam, its boundary-layer solutions are non-zero at the original boundaries and damage locations because damage introduces new boundaries. At a damage location, the boundary-layer solution of slope changes sign, and the boundary-layer solution of displacement peaks up or dimples down. The theoretical background is shown in detail. Noise and different types of damage are simulated to show how they affect damage locating curves. Experiments are performed on several different beams with different types of damage, including surface slots, edge slots, surface holes, internal holes, and fatigue cracks. Experimental results show that this damage detection method is sensitive and reliable for locating small damages in beams.

Keywords: Boundary effect detection; Operational deflection shape; Scanning laser vibrometer

1. Introduction

In recent years, structural health monitoring using dynamic response has been shown to be a feasible approach for detecting and locating damage (Doebling et al., 1996). A crack in a structure introduces local flexibilities and changes dynamic characteristics of the structure. Hence, the crack location and size can be determined from the change of dynamic characteristics (Kam and Lee, 1994; Doebling et al., 1996). To detect small cracks using structural dynamic response, high-frequency excitation is necessary in order to reduce wavelengths, to increase curvatures, and to activate the gaping of cracks. However, high-frequency deformation shapes require spatially dense and accurate measurements. More seriously, the most popular structural modeling technique, the displacement-based finite-element method, is not accurate in predicting high-frequency response because internal bending moments and shear forces are not formulated to be

* Corresponding author. Tel.: +1-573-884-1474; fax: +1-573-884-5090.
E-mail address: paip@missouri.edu (P.F. Pai).

0020-7683/01/$ - see front matter
PII: S0020-7683(00)00274-2

continuous at nodes. In other words, the two major problems in dynamics-based damage detection are (1) how to reduce spatial aliasing in dynamic response measurements and (2) how to extract clear damage signals from the measured dynamic response without using a structural model for reference. Hence, a tool for high-density measurements and an accurate model-independent damage detection method is really necessary for performing practical structural damage detection.

Spatial aliasing is due to insufficient dynamic response measurements. A scanning laser vibrometer provides a unique solution to this problem because of its non-contact (measuring structural velocities by checking the frequency shift of a backscattered laser beam), remote (up to 30 m away), large-area scanning (up to $40^\circ \times 40^\circ$), dense (up to 512×512 points), high frequency bandwidth (0.2 Hz to 200 kHz), and accurate (a velocity resolution up to 0.1 μm/s) measurement capabilities. To extract clear damage signals from the measured large amount of dynamic response data, a newly developed boundary effect detection (BED) method is able to extract damage-induced boundary-layer effects from structural operational deflection shapes (ODSs) measured by a scanning laser vibrometer (Pai and Jin, 2000). An ODS is the deflection shape of a structure subjected to a single-frequency harmonic excitation. When the excitation frequency is close to an isolated natural frequency of the structure, the ODS is dominated by the corresponding mode shape. If it is not an isolated natural frequency, the ODS may consist of multiple mode shapes. The BED method is a model-independent method; it uses a sliding-window least-squares curve-fitting method to decompose an ODS into central and boundary-layer solutions. Because damage introduces new boundaries to a structure, boundary-layer solutions exist around damages and original boundaries and hence can reveal damage locations. Experiments have been performed to verify the capability of this BED method in locating surface slots and stiffened sections (Pai and Jin, 2000). The results indicate that the BED method seems more sensitive and reliable than other dynamics- or deformation-based methods, including digital shearography (Sirohi et al., 1999), curvature methods, and strain energy methods. However, some difficulties and limitations have been observed.

This work is to provide in-depth studies of the BED method in locating different types of damage, to improve this method, and to experimentally verify the accuracy of this method in detecting multiple damages. Next, we derive the BED method of Pai and Jin, 2000 using an alternative approach.

2. Boundary effect detection method

To show the theory without complex derivations we consider one-dimensional structures (i.e., beams) and assume that the obtained ODS consists of only one mode shape. We will show that the BED method works for flexural, torsional, and longitudinal ODSs. Next, we show the theoretical background of using flexural ODSs to detect damage.

2.1. Flexural vibration

For a beam the equation governing flexural vibrations is given by

$$(EIw'')'' + c\dot{w} + m\ddot{w} = f(x,t), \tag{1}$$

where E is Young's modulus, I, the area moment of inertia, c, the damping coefficient, m, the mass per unit length, f, the distributed external load, x, the spatial coordinate, t, the time, w the transverse displacement, $(\ )' \equiv \partial(\ )/\partial x$, and $(\dot{}\ ) \equiv \partial(\ )/\partial t$. The ith mode shape W_i of a uniform beam is the free undamped deflection shape vibrating at the ith natural frequency ω_i and is given by

$$W_i(x) = c_1 \cos\beta_i x + c_2 \sin\beta_i x + c_3 \cosh\beta_i x + c_4 \sinh\beta_i x, \quad \beta_i \equiv \left(\frac{m\omega_i^2}{EI}\right)^{1/4}, \tag{2}$$

where the coefficients c_i can be determined using boundary conditions and β_i is determined by the corresponding frequency equation.

For any boundary conditions, Dugundji et al. (1988) showed that, when the mode number i is not small,

$$W_i(x) = c_1 \cos \beta_i x + c_2 \sin \beta_i x + \bar{c}_3 e^{-\beta_i x} + \bar{c}_4 e^{-\beta_i (L-x)}, \tag{3}$$

where L is the beam length.

In solid mechanics, St. Venant's principle implies that a system of loads having zero resultant forces and moments (i.e., a self-equilibrated stress system) produces a displacement field that is negligible at points far away from the loading end (Iesan, 1987). The deformations caused by such a self-equilibrated load system have a short decay length and are called boundary-layer solutions (Iesan, 1987; Giavotto et al., 1983). On the other hand, the deformations at points away from the ends where nontrivial stress resultants are applied are called central solutions (Iesan, 1987; Giavotto et al., 1983). For a structure under free vibration, external loads are acting only at its boundaries. Hence, boundary-layer solutions exist only around the boundaries, and their magnitudes depend on the actual distributions of constraints at the boundaries.

We note that the third and fourth terms in Eq. (3) are boundary-layer solutions because these two terms are zero at a point away from the left and right boundaries (i.e., $x = 0, L$). It indicates that $\cosh \beta_i x$ and $\sinh \beta_i x$ in Eq. (2) are due to boundary constraints, and $\cos \beta_i x$ and $\sin \beta_i x$ are central solutions. To extract boundary-layer solutions from an ODS, we will use a sliding-window least-squares curve-fitting method and a moving coordinate $\bar{x}$ which is defined as

$$\bar{x} \equiv x - x_{\mathrm{m}}. \tag{4}$$

Here x_{m} is the location of the point under observation. Using Eq. (4) one can rewrite Eq. (2) as

$$\begin{aligned} W(x) &= c_1 \cos(\beta x_{\mathrm{m}} + \beta \bar{x}) + c_2 \sin(\beta x_{\mathrm{m}} + \beta \bar{x}) + c_3 \cosh(\beta x_{\mathrm{m}} + \beta \bar{x}) + c_4 \sinh(\beta x_{\mathrm{m}} + \beta \bar{x}) \\ &= C_1 \cos(\beta \bar{x}) + C_2 \sin(\beta \bar{x}) + C_3 \cosh(\beta \bar{x}) + C_4 \sinh(\beta \bar{x}), \end{aligned} \tag{5}$$

where the subindex i is dropped to simplify the notation, and

$$\begin{aligned} &C_1 \equiv \sqrt{c_1^2 + c_2^2} \cos(\beta x_{\mathrm{m}} - \phi), \qquad C_2 \equiv -\sqrt{c_1^2 + c_2^2} \sin(\beta x_{\mathrm{m}} - \phi), \\ &C_3 \equiv \sqrt{c_3^2 + c_4^2} \cosh(\beta x_{\mathrm{m}} + \psi), \qquad C_4 \equiv \sqrt{c_3^2 + c_4^2} \sinh(\beta x_{\mathrm{m}} + \psi), \\ &\tan \phi \equiv \frac{c_2}{c_1}, \qquad \tanh \psi \equiv \frac{c_4}{c_3}. \end{aligned} \tag{6}$$

To find the coefficients C_i $(i = 1, 2, 3, 4)$ for the point at $\bar{x} = 0$ (i.e., $x = x_{\mathrm{m}}$) we use the data points around $x = x_{\mathrm{m}}$ to minimize the fitting error. If W_i denotes $W(\bar{x}_i)$ and Y_i denotes the experimental data at $\bar{x}_i$, we define the fitting error Error as

$$\mathrm{Error} = \sum_{i=-N}^{N} \alpha_i (W_i - Y_i)^2, \tag{7}$$

where the total number of points used is $2N + 1$, and α_i is a weighting factor. In this work, we choose to use

$$\alpha_i = \frac{1}{1 + |\, 99 i/N \,|}.$$

The four equations to determine C_i for the point at $\bar{x} = 0$ are given by

$$\frac{\partial \mathrm{Error}}{\partial C_i} = 0, \quad i = 1, 2, 3, 4. \tag{8}$$

After C_i are determined, one can obtain W, W', W'', and W''' for the point at $\bar{x} = 0$ by using the following equations:

$$\begin{aligned} W(0) &= C_1 + C_3, \\ W'(0) &= (C_2 + C_4)\beta, \\ W''(0) &= (-C_1 + C_3)\beta^2, \\ W'''(0) &= (-C_2 + C_4)\beta^3. \end{aligned} \tag{9}$$

From Eqs. (9) and (5) and the observations on Eq. (3) we know that C_1 represents the central solution of displacement (at $x = x_m$), C_3 represents the boundary-layer solution of displacement caused by boundary constraints, $C_2\beta$ represents the central solution of slope, and $C_4\beta$ represents the boundary-layer solution of slope. Damage creates new boundaries to a structure and introduces new boundary-layer solutions to the structure. When there is no damage at a point away from boundaries, C_3 and C_4 should be zero. If C_3 and C_4 are not zero at a point away from boundaries or C_3 and C_4 show sudden change, it implies that boundary conditions are changed due to damage and/or non-uniform material distribution at that point.

It follows from Eqs. (9) and (2) that the maximum elastic energy density Π is given by

$$\Pi = \tfrac{1}{2}EIW''(0)^2 = \tfrac{1}{2}EI(C_3 - C_1)^2\beta^4 = \tfrac{1}{2}m\omega^2(C_3 - C_1)^2. \tag{10}$$

Moreover, under steady-state harmonic vibrations the maximum kinetic energy density K is given by

$$K = \tfrac{1}{2}m(W(0)\omega)^2 = \tfrac{1}{2}m\omega^2(C_3 + C_1)^2. \tag{11}$$

Hence, the difference between these two energy densities is

$$K - \Pi = 2m\omega^2 C_1 C_3. \tag{12}$$

In other words, C_1C_3 is proportional to $K - \Pi$. Hence, if there is no damage, $C_3 = 0$ and hence $K - \Pi = 0$ at a point away from boundaries. This is a useful phenomenon to be used for identifying damage locations.

It is noticed that the sectional standard deviation (SSD) and standard deviation (SD) of the fitting process are also useful for indicating damage. The SSD is computed as

$$\mathrm{SSD} \equiv \sqrt{\frac{\sum_{i=-N}^{N}[W(\bar{x}_i) - Y(\bar{x}_i)]^2}{2N+1}}. \tag{13}$$

The overall SD is computed after the C_i for every point on the beam are obtained, and it is computed as

$$\mathrm{SD} \equiv \sqrt{\frac{\sum_{m=1}^{M}[W(x_m) - Y(x_m)]^2}{M}}, \tag{14}$$

where M is the total number of points measured along the beam.

The β in Eq. (5) needs to be estimated before using the linear sliding-window least-squares method shown in Eqs. (7) and (8). To determine β for a high-frequency deflection shape one can plot the experimental ODS and then pick up a representative wavelength λ to obtain $\beta = 2\pi/\lambda$. For a low-frequency deflection shape (e.g., $i < 3$ in Eq. (3)), it is difficult to obtain an accurate estimation of β from the ODS. However, one can use the theoretical value of a beam with boundary conditions similar to the one under study. It is shown later that for finding damage locations, the proposed method does not require an accurate estimation of β. Moreover, if the estimated β is not correct, the sectional standard deviation of the curve fitting and boundary-layer solutions will show periodic change. Hence, it is easy to know whether the estimated β is correct, and, if necessary, one can revise the estimation and rerun the signal processing. Furthermore, if necessary, one can use a nonlinear sliding-window least-squares method (Pai and Jin, 2000)

to find β and C_i simultaneously. After β is computed using the nonlinear curve fitting, one can estimate the change of m/EI, Eq. (2) to quantify the damage.

Because polynomials are very often used in curve-fitting, let us consider that

$$W(x) = C_1 + C_2\bar{x} + C_3\bar{x}^2 + C_4\bar{x}^3. \tag{15}$$

It follows from Eq. (15) that

$$W(0) = C_1, \qquad W'(0) = C_2, \qquad W''(0) = 2C_3, \qquad W'''(0) = 6C_4. \tag{16}$$

One can also show that

$$K - \Pi = \tfrac{1}{2}m(\omega C_1)^2 - \tfrac{1}{2}EI(2C_3)^2 = \tfrac{1}{2}m\omega^2(C_1^2 - 4\beta^{-4}C_3^2), \tag{17}$$

where Eq. (2) is used. We note that, if polynomials are used for the curve-fitting, the boundary-layer solutions cannot be separated from the central solutions. Although β is not needed in obtaining Eq. (16), the calculation of $K - \Pi$ still requires the estimation of β because the structural properties m and EI are not required in the BED method and are assumed to be unknown.

2.2. Torsional vibration

For a uniform isotropic torsional bar with y and z being the principal axes of cross-sections, one can use Vlasov's beam theory (Vlasov, 1961) to obtain

$$EJ_\psi\phi^{iv} - GJ_\phi\phi'' + J_0\ddot{\phi} = 0, \tag{18}$$

where

$$\begin{aligned}
&\psi(y,z) \equiv yz - \frac{J_{23}}{J_2}y - \frac{J_{32}}{J_3}z,\\
&J_2 \equiv \int_A y^2\mathrm{d}A, \qquad J_3 \equiv \int_A z^2\mathrm{d}A, \qquad J_{23} \equiv \int_A y^2z\mathrm{d}A, \qquad J_{32} \equiv \int_A yz^2\mathrm{d}A,\\
&J_\psi \equiv \int_A \psi^2\mathrm{d}A, \qquad J_\phi \equiv \frac{4J_2J_3}{J_2+J_3}, \qquad J_0 \equiv \int_A \rho(y^2+z^2)\mathrm{d}A.
\end{aligned} \tag{19}$$

Here E is Young's modulus, G, the shear modulus, A, the cross-sectional area, ψ, the out-of-plane torsional warping function, ϕ, the torsional angle, and ρ the mass density per unit volume. We note that the fourth-order derivative term is due to the torsional warping effect.

The mode shape Φ of torsional vibrations can be shown to have the following form:

$$\Phi(x) = c_1\cos(\beta x) + c_2\sin(\beta x) + c_3\cosh(\beta_1 x) + c_4\sinh(\beta_1 x), \tag{20}$$

where

$$\beta \equiv \sqrt{\frac{-GJ_\phi + \sqrt{G^2J_\phi^2 + 4EJ_\psi J_0\omega^2}}{2EJ_\psi}}, \qquad \beta_1 \equiv \sqrt{\frac{GJ_\phi + \sqrt{G^2J_\phi^2 + 4EJ_\psi J_0\omega^2}}{2EJ_\psi}}. \tag{21}$$

Here ω is the natural frequency. Hence, equations similar to Eqs. (9) and (12) can be derived.

2.3. Longitudinal vibration

Similar to the governing equation of torsional vibrations, in-plane warping restraints introduce higher-order derivatives to the governing equation of longitudinal vibrations (Giavotto et al., 1983). Hence, the equation governing longitudinal vibrations of a bar has the form:

$$EA_{\mathrm{w}}u^{iv} - EAu'' + \rho A\ddot{u} = 0, \tag{22}$$

where u is the longitudinal displacement and A_{w} is a nondimensional parameter accounting for in-plane warping restraints.

The mode shape U of longitudinal vibrations can be shown to have the following form:

$$U(x) = c_1\cos(\beta x) + c_2\sin(\beta x) + c_3\cosh(\beta_1 x) + c_4\sinh(\beta_1 x), \tag{23}$$

where

$$\beta \equiv \sqrt{\frac{-EA + \sqrt{E^2A^2 + 4EA_{\mathrm{w}}\rho A\omega^2}}{2EA_{\mathrm{w}}}}, \qquad \beta_1 \equiv \sqrt{\frac{EA + \sqrt{E^2A^2 + 4EA_{\mathrm{w}}\rho A\omega^2}}{2EA_{\mathrm{w}}}}. \tag{24}$$

Here ω is the natural frequency. Hence, equations similar to Eqs. (9) and (12) can be derived.

3. Numerical simulation

Damage detection is an inverse problem; it is difficult to obtain a unique solution. Considering both solution nonuniqueness and experimental noise at the same time will make it very difficult to develop damage detection methods. Here, we first perform studies using numerical mode shapes without noise to get a clear idea of what parameters are sensitive to damage in the proposed method. Then, we add normally distributed random noise to the data to check the robustness of the method. Experimental results are presented in Section 4.

To obtain numerical mode shapes of a beam with a crack, we model the beam using three beam segments, as shown in Fig. 1. We consider a clamped–clamped aluminum beam with $L = 24.125''$, $b = 0.743''$, and $h = 0.188''$. Young's modulus $E = 9.15 \times 10^6$ psi, and the mass density $\rho = 5.2$ slug/ft^3. A correction factor $k(<1)$ can be used to account for the stress concentration effect around the slot by reducing the bending stiffness of the slotted segment to be $kEb(h-2d)^3/12$. However, the value of k highly depends on the geometry of the crack tip (Shen and Pierre, 1990), and it is difficult to predict the actual value of k of a crack. Although the stress concentration increases the bending curvature around a crack and makes the job of finding damage easier (Pai and Jin, 2000), in the following numerical simulations, we will neglect the stress concentration effect and assume $k = 1$ in order to simplify the comparison of different damage effects. The ith mode shape of the jth beam segment is presented as

$$\widehat{W}_j(x) = A_j\cos\beta_j x + B_j\sin\beta_j x + C_j\cosh\beta_j x + D_j\sinh\beta_j x. \tag{25}$$

Each beam segment has its own β_j but there is only one ith natural frequency. Because of the use of hyperbolic functions $\cosh\beta x$ and $\sinh\beta x$, the origin of x is set at the center of each beam segment to reduce the chance of numerical singularity. Using the boundary conditions and continuity of displacements, slopes, bending moments, and shear forces at the junction points, one can solve for the β_j for each beam segment and the ith natural frequency.

Next, we show the influences of different damages and parameters on damage locating curves.

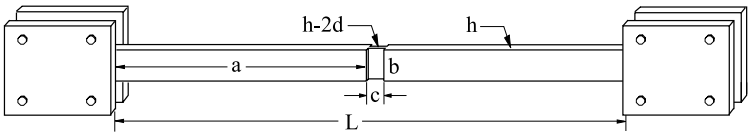

Fig. 1. A clamped–clamped aluminum beam with a symmetric open crack.

3.1. Surface slots

Fig. 2 shows the results of processing the seventh mode shape of the beam shown in Fig. 1 with a symmetric crack at $x = a + c/2 = 0.5L$, which is actually a narrow slot. The crack width $c = 0.055''$ and the crack depth $d = 0.15h = 0.0282''$. Here $N = 5$ (Eq. (7)) and $\Delta x = L/200$ (the distance between two adjacent points measured) are used. Moreover, W_m denotes the maximum value of the ODS. If no crack, the boundary-layer solutions C_3 and C_4 should be zero at points away from boundaries. However, the crack causes a sign change of C_4 (slope due to boundary constraints), a peak on C_3 (displacement due to boundary constraints), and a peak on SSD at the exact crack location. We note that, if $-W(x)$ is processed, the crack causes a dimple on C_3, instead of a peak. However, the use of $-W(x)$ causes the same dimple on $C_1 * C_3$ because $C_1 * C_3$ is proportional to the difference between the kinetic and elastic energy densities (Eq. (12)), which is not affected by the sign of $W(x)$. Hence, it is more convenient to use $C_1 * C_3$ than to use C_3 for locating damage. The dimple on $C_1 * C_3$ indicates that the kinetic energy is less than the elastic energy around the crack. Because m and EI are assumed to be constant in the signal processing, the actual large curvature around the crack causes the estimated elastic energy to be high and hence $K - \Pi < 0$. Fig. 2(a) shows that the curve-fitted ODS (the line connecting the dots) fits well with the numerical ODS (the dots). We note that it is difficult to find the crack location from the ODS. On the other hand, $C_3 - C_1$ (i.e., W'', see Eq. (9), the thick line) and $C_4 - C_2$ (i.e., W''', the thin line) have significant changes around the crack. However, it will be shown later in Fig. 9 that these changes are difficult to see when there is measurement noise.

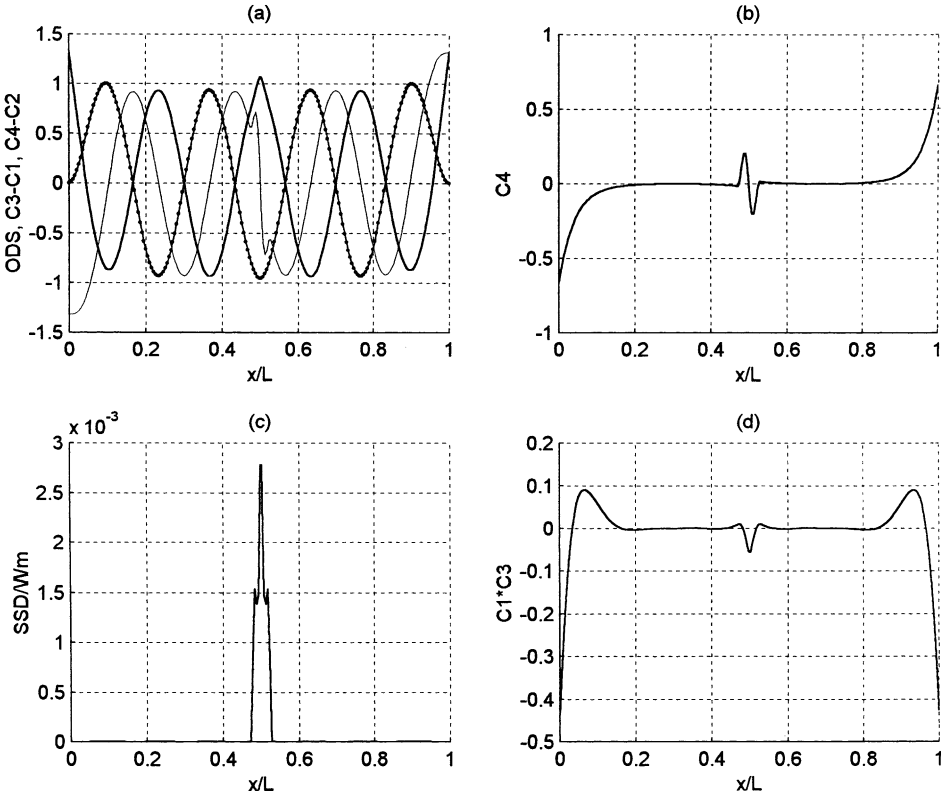

Fig. 2. Numerical damage locating curves when there is a center symmetric crack with $c = 0.055''$ and $d = 0.15h$: (a) ODS (dots), fitted ODS (solid line connecting dots), $C_3 - C_1$ (thick line), and $C_4 - C_2$ (thin line), (b) C_4, (c) SSD/W_m, and (d) $C_1 * C_3$.

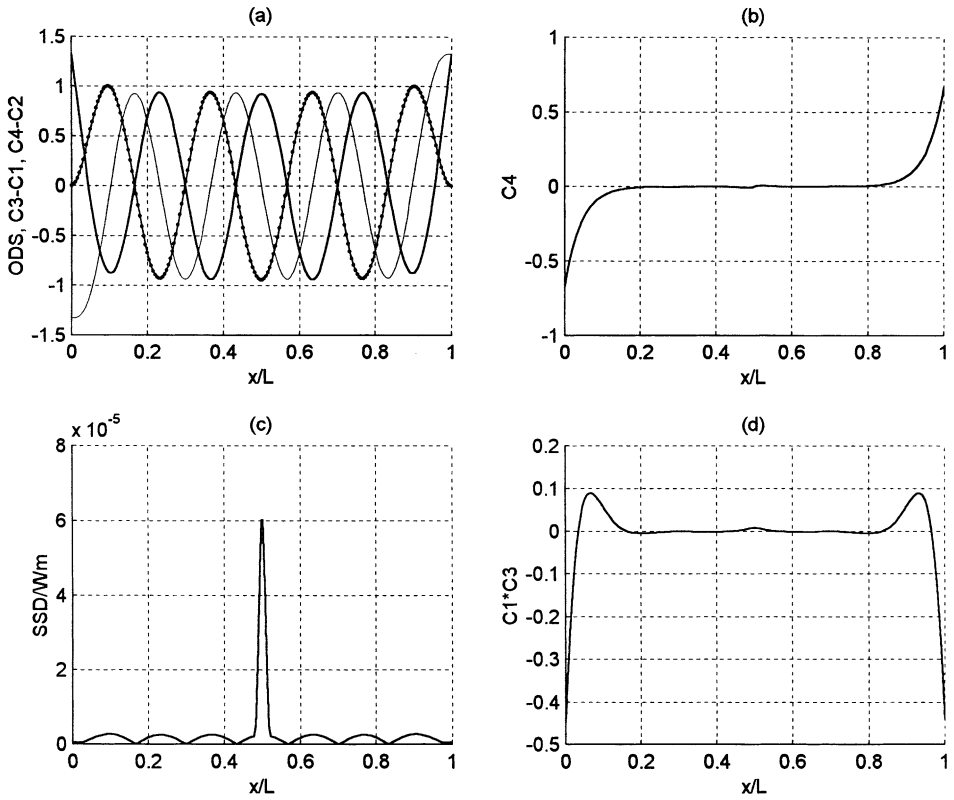

Fig. 3. Numerical damage locating curves when the mass density m of the segment between $x = 0.5L - 0.0275''$ and $x = 0.5L + 0.0275''$ is only 2% of the other two segments: (a) ODS, fitted ODS, $C_3 - C_1$, and $C_4 - C_2$, (b) C_4, (c) SSD/W_m, and (d) $C_1 * C_3$.

If the mass density m of the beam segment between $x = a$ and $x = a + c$ is not accordingly reduced, the results are almost the same as those in Fig. 2. Fig. 3 shows the results when the crack depth $d = 0.49h$, $c = 0.055''$, m of the slotted segment is accordingly reduced, and EI is kept the same for all three segments. $N = 5$ and $\Delta x = L/200$ are used. The peak on $C_1 * C_3$ indicates that the kinetic energy is larger than the elastic energy around $x = a + c/2$. Because m and EI are assumed to be constant in the signal processing, the actual large displacement around $x = a + c/2$ causes the estimated kinetic energy to be large and hence $K - \Pi > 0$. We note that, although the total crack depth $2d = 0.98h$, the sign change of C_4, the peak on $C_1 * C_3$, and the peak on SSD are small. This reveals that flexural mode shapes are mainly controlled by the bending stiffness EI and the loss of mass due to a surface crack has insignificant influence. We also note that it is impossible to locate damage using $C_3 - C_1$ and $C_4 - C_2$ in Fig. 3(a).

3.2. Added lumped masses

Fig. 4 shows the results when there is no crack and a lumped mass of $0.0114mL$ is added at $x = 0.5L$. $N = 5$ and $\Delta x = L/200$ are used here. We note that $C_3 - C_1$ and $C_4 - C_2$ do not have significant sudden change around the lumped mass, and it is difficult to locate the lumped mass. On the other hand, the sign change of C_4, the peak on SSD, and the dimple on $C_1 * C_3$ clearly locate the lumped mass, and their shapes are different from those due to a crack, as shown in Fig. 2. Because m and EI are assumed to be constant in

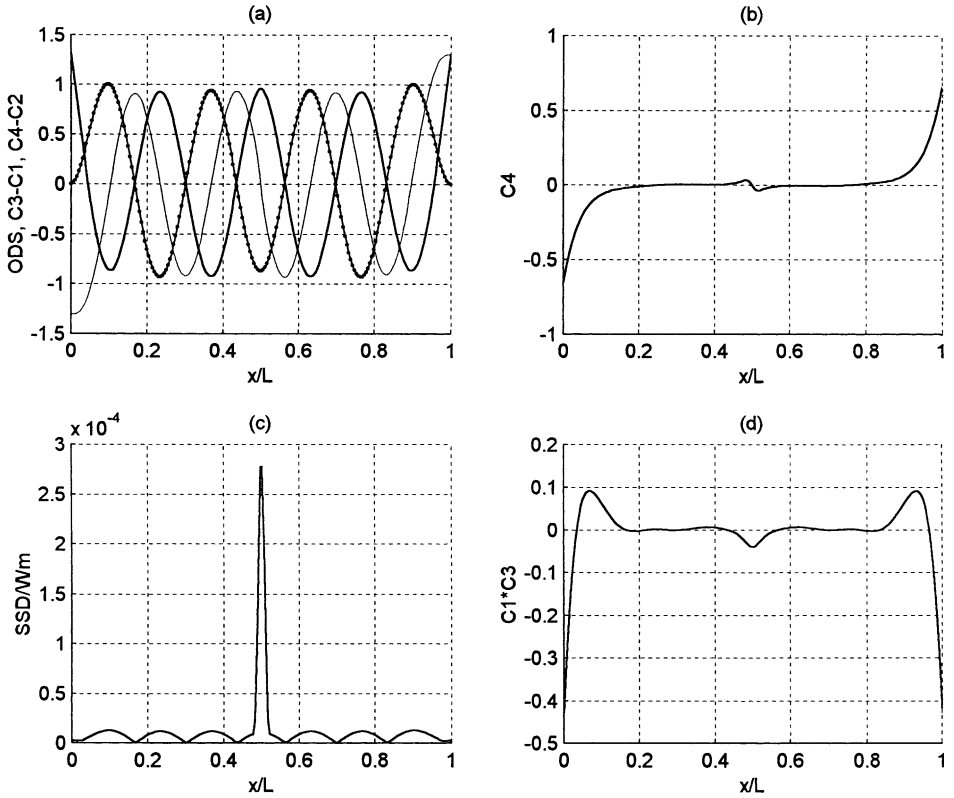

Fig. 4. Numerical damage locating curves when a lumped mass of $0.0114mL$ is added at $x = 0.5L$: (a) ODS, fitted ODS, $C_3 - C_1$, and $C_4 - C_2$, (b) C_4, (c) $\mathrm{SSD}/W_{\mathrm{m}}$, and (d) $C_1 * C_3$.

the signal processing, the actual small displacement around $x = 0.5L$ causes the estimated kinetic energy to be small and hence $K - \Pi < 0$ and a dimple appears on $C_1 * C_3$.

3.3. Added stiffeners

Fig. 5 shows the results when there is no crack and two massless stiffeners having a thickness of $2.5h$ and a width of $0.743''(= b)$ are symmetrically added to the top and bottom of the beam between $x = 0.5L - 0.0275''$ and $x = 0.5L + 0.0275''$. The peak on $C_1 * C_3$ indicates that the elastic energy is less than the kinetic energy around $x = 0.5L$. Because m and EI are assumed to be constant in the signal processing, the actual small curvature around $x = 0.5L$ causes the estimated elastic energy to be small and hence $K - \Pi > 0$. Figs. 3 and 5 show that adding a massless stiffener is similar to but not the same as taking away some mass from the beam. Fig. 6 shows the results if the two symmetric stiffeners have the same mass density as the aluminum beam. $N = 5$ and $\Delta x = L/200$ are used in Figs. 5 and 6. Fig. 6 is the summation of Figs. 4 and 5. Moreover, Figs. 6 and 2 show that adding a stiffener does not behave exactly opposite to cutting a slot.

3.4. Through-the-width internal holes

Fig. 7 shows the damage locating curves when there is a rectangular through-the-width hole having a thickness of $0.7h$ and between $x = 0.5L - 0.0275''$ and $x = 0.5L + 0.0275''$. $N = 5$ and $\Delta x = L/200$ are used.

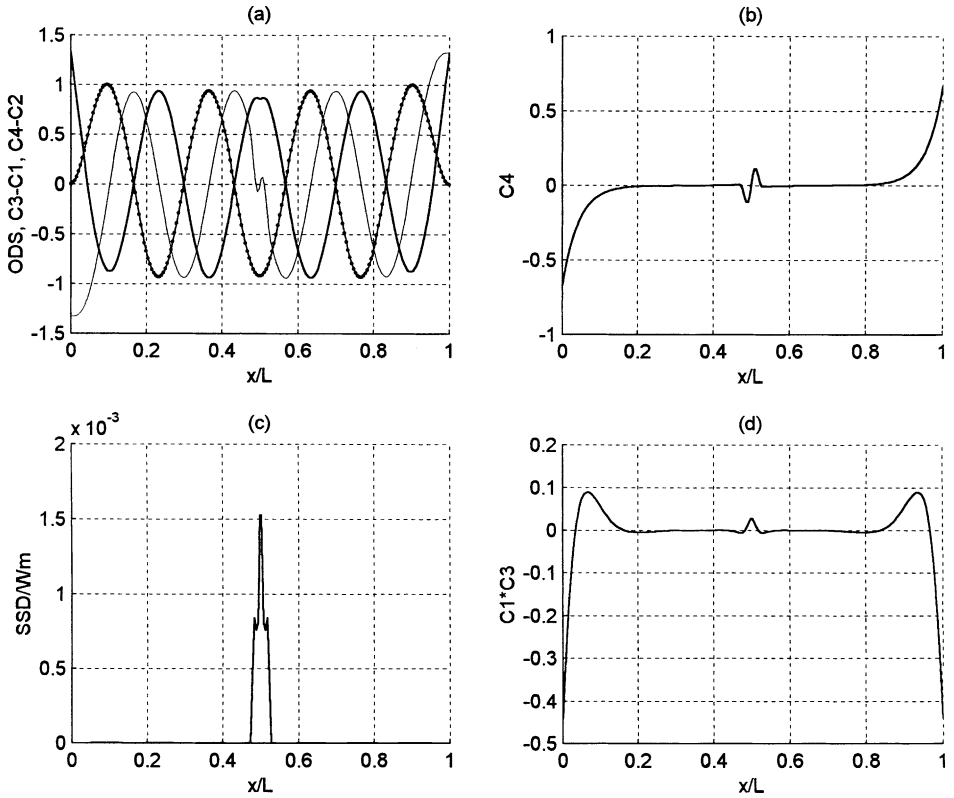

Fig. 5. Numerical damage locating curves when two massless stiffeners with a thickness of $2.5h$ and a width of $0.743''$ are symmetrically added between $x = 0.5L - 0.0275''$ and $x = 0.5L + 0.0275''$: (a) ODS, fitted ODS, $C_3 - C_1$, and $C_4 - C_2$, (b) C_4, (c) SSD/W_m, and (d) $C_1 * C_3$.

The dimple on $C_1 * C_3$ in Fig. 7(d) is much smaller than that in Fig. 2(d). It shows that internal holes are more difficult than surface slots to be detected using transverse vibration ODSs. The reduction of bending stiffness due to an internal hole is smaller than that due to a surface crack because internal holes are in low bending stress areas. On the other hand, the reduction of mass is determined only by the volume of the cut-out, not the location along the thickness direction.

3.5. Side slots

Fig. 8 shows the damage locating curves when there are two symmetric side slots having a depth of $0.15b$ and a width of $0.055''$ at $x = 0.5L$. $N = 5$ and $\Delta x = L/200$ are used. One can see that these damage locating curves are similar to those caused by an internal hole, as shown in Fig. 7.

3.6. Noise

For real cases, damage locating curves are affected by experimental noise in different degree. Fig. 9 shows the results of processing the seventh mode shape of the beam shown in Fig. 1 with a center symmetric crack having $c = 0.055''$ and $d = 0.15h$. This case is the same as that presented in Fig. 2 except that we add to the mode shape a normally distributed random noise having a standard deviation of 0.2% of W_m. Here $N = 5$

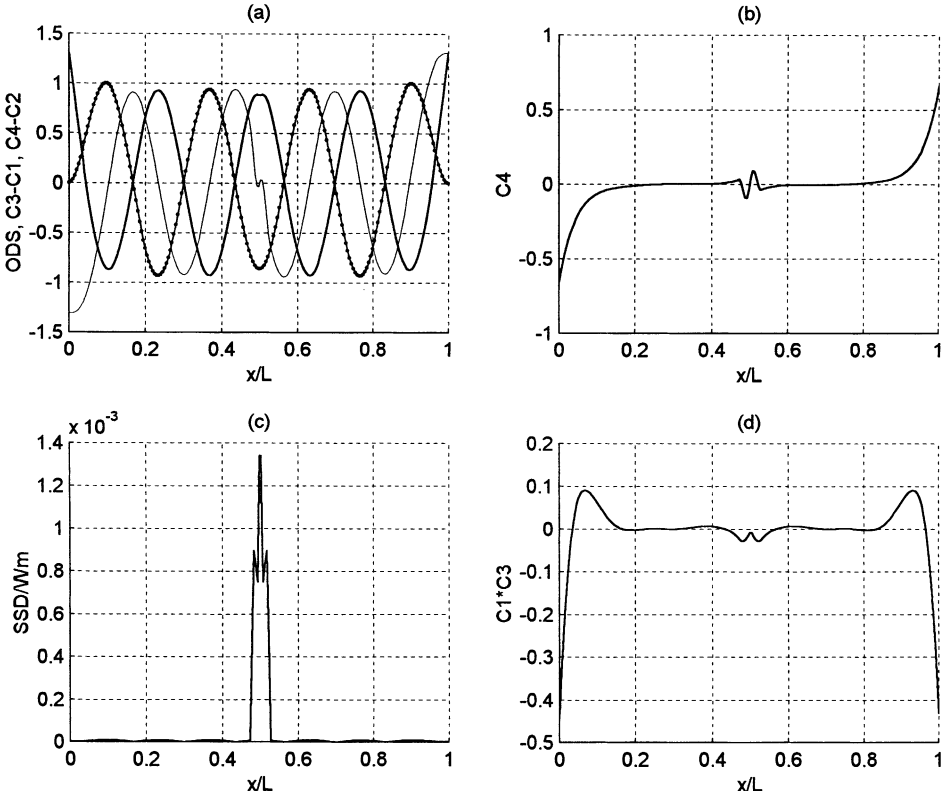

Fig. 6. Numerical damage locating curves when the thickness of the segment between $x = 0.5L - 0.0275''$ and $x = 0.5L + 0.0275''$ is $6h$: (a) ODS, fitted ODS, $C_3 - C_1$, and $C_4 - C_2$, (b) C_4, (c) SSD/W_m, and (d) $C_1 * C_3$.

and $\Delta x = L/200$ are used. The sliding-window length is $2N\Delta x = L/20$, and it is about 0.175λ, where λ is the wavelength of the ODS. We note that it becomes more difficult to locate the crack using the curves of $C_3 - C_1$ and $C_4 - C_2$. However, the sign change of C_4 at the crack location is still more significant than those at other locations, and the dimple on $C_1 * C_3$ and the peak on SSD at the crack location are still clear.

3.7. Sliding-window length

To show the influence of the sliding-window length (i.e., $2N\Delta x$) used in the curve fitting we increase Δx from $L/200$ in Fig. 9 to $2L/200$ in Fig. 10. Figs. 9 and 10 show that increasing the window length smooths out all damage locating curves, reduces the dimple on $C_1 * C_3$, reduces the sign change of C_4, and increases the peak on SSD. It becomes more difficult to locate damage using $C_3 - C_1$ and $C_4 - C_2$ when the window length increases, but the dimple on $C_1 * C_3$, the sign change of C_4, and the peak on SSD still clearly indicate the crack location.

We note that $C_3 - C_1$ requires about the same, or a little bit larger, window length than $C_3 * C_1$ to smooth out the curve. Because C_2 is much larger than C_4 and C_2 is wavy (see Eq. (6)), C_4 requires a little bit larger window length than $C_4 - C_2$ to smooth out the curve. All numerical simulations show that the required sliding-window length increases in the following order: (1) the difference of kinetic and elastic energy densities ($C_1 * C_3$), (2) the curvature ($C_3 - C_1$), (3) the central solution of slope (C_2), (4) the derivative of curvature ($C_4 - C_2$), (5) the boundary-layer solution of slope (C_4), (6) the fitting error (SSD), and (7) the β if

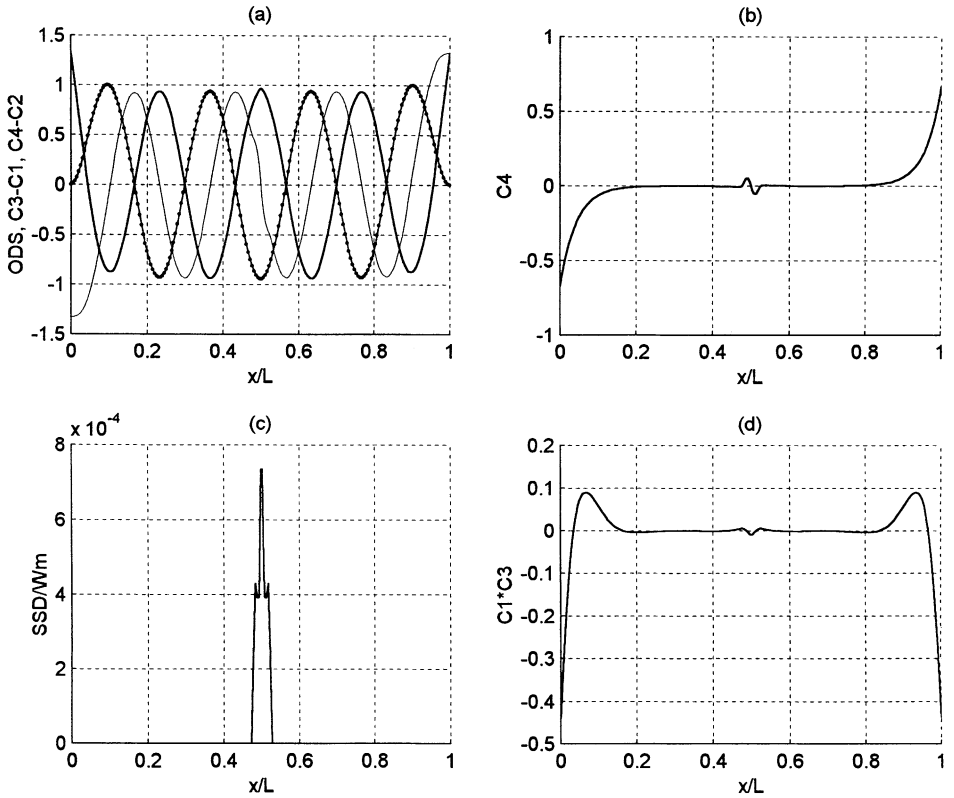

Fig. 7. Numerical damage locating curves when there is a rectangular through-the-width hole having a thickness of $0.70h$ and between $x = 0.5L - 0.0275''$ and $x = 0.5L + 0.0275''$: (a) ODS, fitted ODS, $C_3 - C_1$, and $C_4 - C_2$, (b) C_4, (c) $\mathrm{SSD}/W_{\mathrm{m}}$, and (d) $C_1 * C_3$.

a nonlinear fitting method (Pai and Jin, 2000) is used. When the sliding-window length $2N\Delta x$ increases from a small value, $C_1 * C_3$ becomes smooth and can indicate the damage before $C_4 - C_2$ becomes smooth, and C_4 can still indicate the damage after $C_4 - C_2$ becomes too smooth to show damage. Hence, this method is more sensitive and reliable than damage identification methods using W'' (e.g., energy/curvature methods) and W''' (e.g., digital shearography). We note that, when the sliding-window length $2N\Delta x$ is short, C_i are rough, which may make it difficult to locate damage. On the other hand, when $2N\Delta x$ is large, the boundary-layer effects around the crack are averaged out and it is also difficult to locate damage. However, because every C_i requires a different window length and shows damage locations in a different way, one can perform two analyses using two different window lengths and then overlap the results to reveal damage locations.

Figs. 2–10 show that it is difficult to distinguish damage locating curves caused by different types of damage, especially when noise exists. The use of structural dynamic response to predict the type and degree of damage is an inverse problem and the obtained solution may not be unique, as shown in Figs. 9 and 10. The estimation of the type and degree of damage from the obtained damage locating curves requires more studies.

3.8. Mode number

Fig. 11 shows the results of processing the thirteenth mode shape of the beam shown in Fig. 1 with a center symmetric crack having $c = 0.055''$ and $d = 0.15h = 0.0282''$. Here, we add to the mode shape a

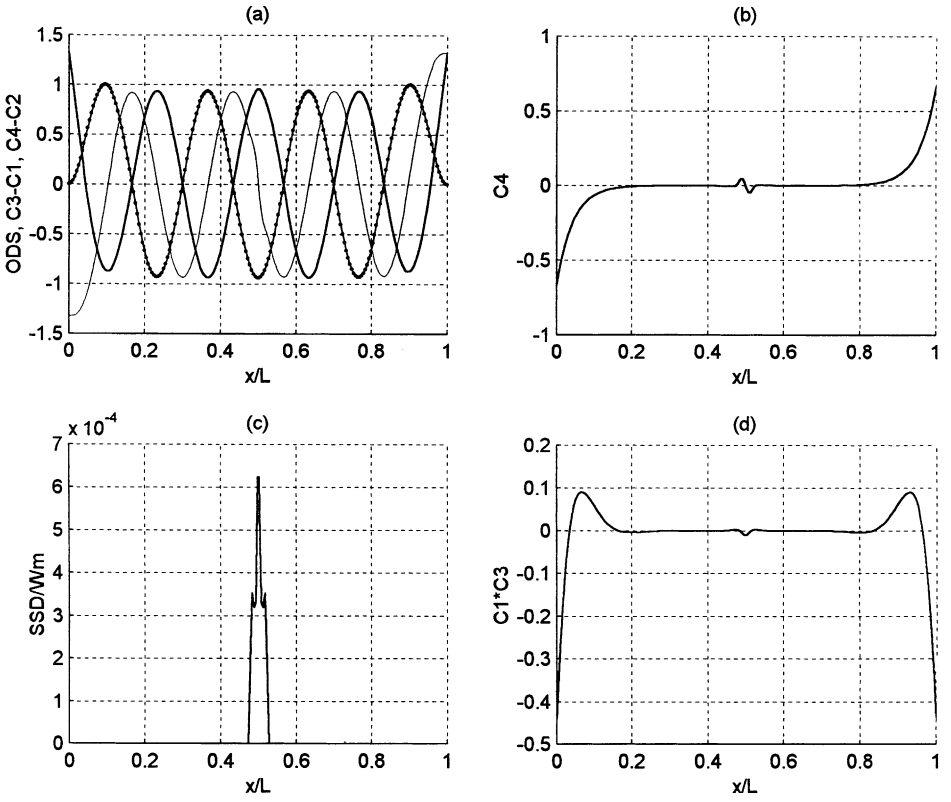

Fig. 8. Numerical damage locating curves when the width of the segment between $x = 0.5L - 0.0275''$ and $x = 0.5L + 0.0275''$ is 0.7*b*: (a) ODS, fitted ODS, $C_3 - C_1$, and $C_4 - C_2$, (b) C_4, (c) SSD/W_m, and (d) $C_1 * C_3$.

normally distributed random noise having a standard deviation of 0.2% of W_m, and $N = 5$ and $\Delta x = L/400$ are used. The sliding-window length is $2N\Delta x = L/40$, and it is about 0.1625λ, where λ is the wavelength of the ODS. We note that the roughness of the damage locating curves is about the same as that in Fig. 9. When the window length increases to $2N\Delta x = L/20$ by using $\Delta x = 2L/400$, the results are shown in Fig. 12. We note that the roughness of the damage locating curves is about the same as that in Fig. 10. This reveals that the roughness of damage locating curves is determined by the ratio of the window length and the wavelength, i.e., $2N\Delta x/\lambda$. Figs. 10 and 12 show that using high-frequency ODSs gives more localized and clear damage locating curves. However, a high-frequency ODS requires more points to be measured in order to show a smooth deflection shape.

3.9. Damage location

Figs. 13–15 show the damage locating curves of a symmetric crack with $c = 0.055''$ and $d = 0.15h$ at $x = 0.46L$, $x = 0.42L$, and $x = 0.9L$, respectively. $N = 5$ and $\Delta x = L/200$ are used. Figs. 13 and 14 show that, when the crack is at a low curvature area, the peaks and sign changes of damage location curves are small and it is difficult to locate damage. Fig. 15 shows that overlapping the results of two analyses using two different window lengths clearly reveals the damage location even if the damage is in a boundary-layer zone. The thin lines in Fig. 15(b)–(d) are obtained using $N = 5$ and $\Delta x = 2L/200$. If the thin lines in

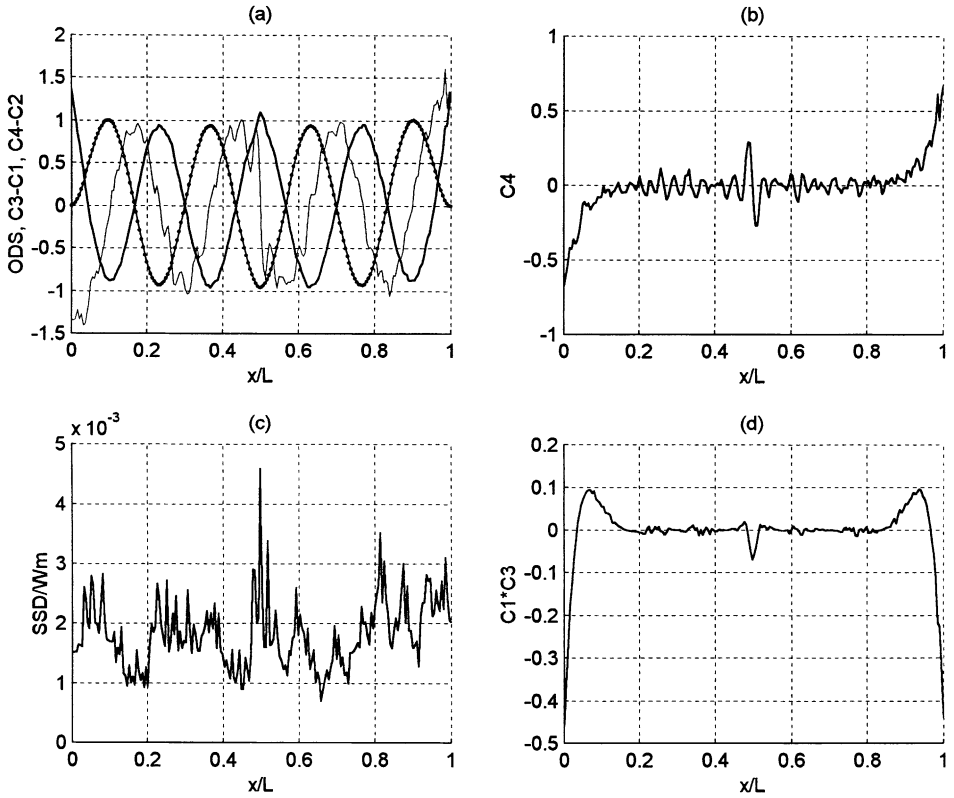

Fig. 9. Numerical damage locating curves when there is a center symmetric crack, $c = 0.055''$, $d = 0.15h$, 0.2% noise is added to the 7th mode shape, $N = 5$, and $\Delta = L/200$: (a) ODS, fitted ODS, $C_3 - C_1$, and $C_4 - C_2$, (b) C_4, (c) SSD/W_m, and (d) $C_1 * C_3$.

Fig. 15(b) and (d) are subtracted from the thick lines, the resulting curve shapes around the crack are similar to those in Fig. 2(b) and (d), which indicates that the damage is a crack.

3.10. β Value

Fig. 16 shows the damage locating curves of a symmetric crack with $c = 0.055''$ and $d = 0.15h$ at $x = 0.5L$, which is the case shown in Fig. 2 except that the estimated β is different from the actual value. $N = 5$ and $\Delta x = L/200$ are used. We note that, if β is erroneously estimated, the BED method still works except that boundary-layer solutions become non-zero everywhere. The thin lines in Fig. 16(b)–(d) are obtained using $N = 5$ and $\Delta x = 2L/200$. Again, overlapping the results of two analyses using two different window lengths clearly reveals the damage location even when the estimated β is wrong.

3.11. Non-uniform distributions of stiffness and mass

Fig. 17 shows the damage locating curves of the beam shown in Fig. 1 with no crack and the segment between $x = 8.0625''$ and $x = 16.0625''$ having a thickness of $1.3h = 0.2444''$. $N = 5$ and $\Delta x = L/200$ are

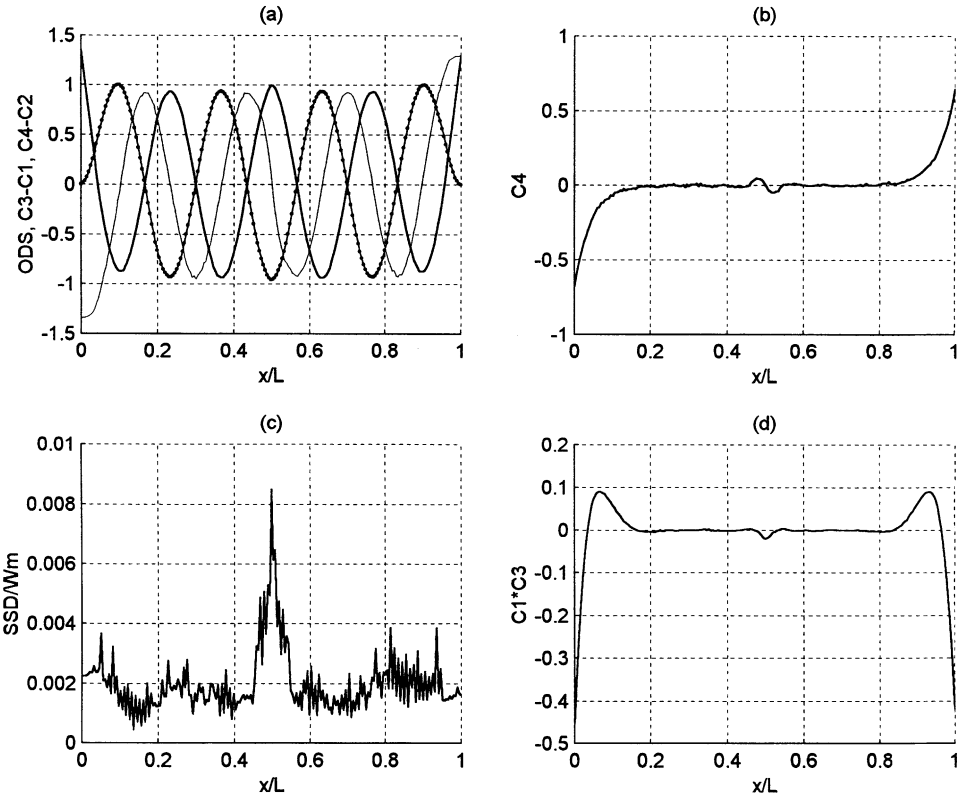

Fig. 10. Numerical damage locating curves when there is a center symmetric crack, $c = 0.055''$, $d = 0.15h$, 0.2% noise is added to the 7th mode shape, $N = 5$, and $\Delta = 2L/200$: (a) ODS, fitted ODS, $C_3 - C_1$, and $C_4 - C_2$, (b) C_4, (c) SSD/W_m, and (d) $C_1 * C_3$.

used. The thin lines in Fig. 17(b)–(d) are obtained using $N = 5$ and $\Delta x = 2L/200$. Again the overlapping of two analyses using two different window lengths clearly reveals the location of the stiffened segment. If the thin lines in Fig. 17(b) and (d) are subtracted from the thick lines, the peaks and/or dimples of ΔC_4 and the sign changes of $\Delta C_1 * C_3$ indicate the edges of the stiffened segment, which are different from damage locating curves of a crack.

4. Experiments

4.1. Experimental setup and procedures

Fig. 18 shows the experimental setup used in measuring ODSs of a beam. A Polytec PSV-200 scanning laser vibrometer is used to measure the velocities of M equally spaced points along the beam, and a lead zirconate titanate (PZT) patch is attached to the root of the beam for excitation. The PZT patch is a quickpack QP10N actuator purchased from ACX (Active Control Experts, Inc., Cambridge, MA.). The quickpack actuator packages piezoceramics in a protective skin (a polyimide coating) with pre-attached electrical leads. The QP10N patch has dimensions $2'' \times 1'' \times .015''$, and its piezo wafer size is $1.81'' \times 0.81'' \times .010''$. The maximum allowable operating voltage of the PZT patch is 200 V.

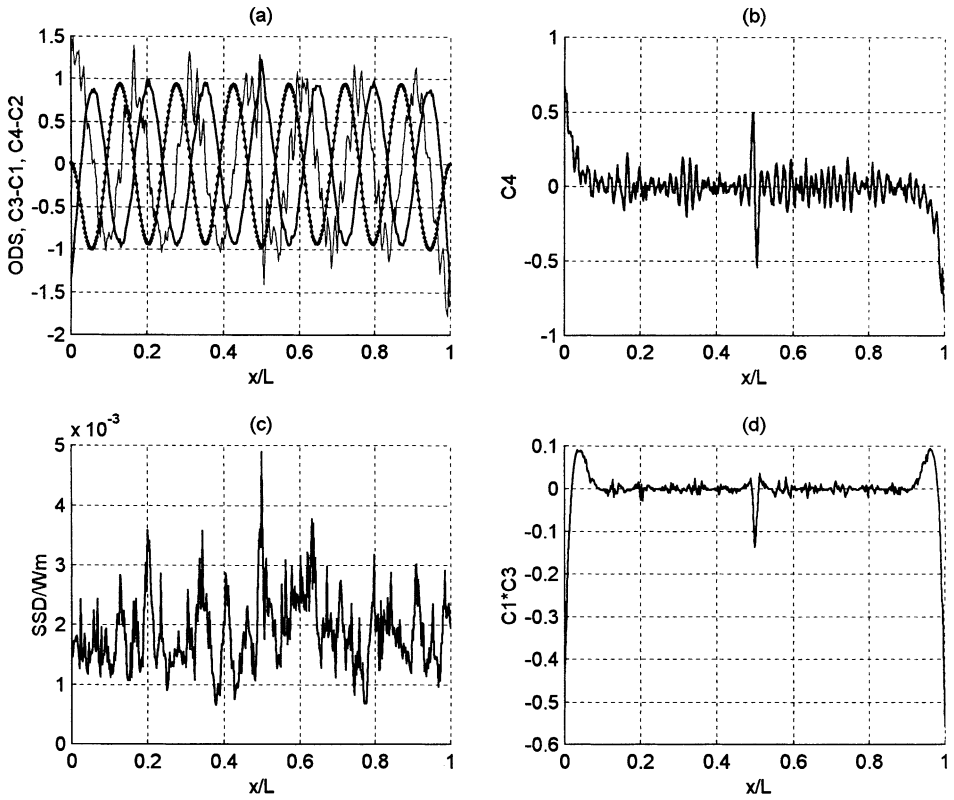

Fig. 11. Numerical damage locating curves when there is a center symmetric crack, $c = 0.055''$, $d = 0.15h$, 0.2% noise is added to the 13th mode shape, $N = 5$, and $\Delta = L/400$: (a) ODS, fitted ODS, $C_3 - C_1$, and $C_4 - C_2$, (b) C_4, (c) SSD/W_m, and (d) $C_1 * C_3$.

The PCB-790 power amplifier magnifies, by 20 times, the sinusoidal voltage from the HP-33120A 15 MHz function generator and sends it to the PZT patch. The OFV-3001-S vibrometer controller controls the rotation of the two mirrors in the OFV-055 scan head and the scanning of the laser beam, and it receives the interferometry created by the backscattered laser beam and the reference laser beam in the OFV-303 sensor head. The output voltage from the HP-33120A function generator is also used as the input signal to channel A of the OFV-3001-S vibrometer controller. The OFV-3001-S controller includes two independently programmable low-pass filters for filtering the signal from the HP-33120A function generator and the signal from the OFV-303 sensor head, respectively. After filtering, these two signals are sent from channels A and B of the controller to the 400 MHz computer system, which is operated by Windows NT and processes the measured data. The video control box controls the swiveling and tilting of the OFV-055 scan head and the focusing of the video camera in the OFV-055 scan head. A standardized composite video signal from the camera is passed via a BNC connection on the video control box to the video input of the computer system.

In the experiments we first perform an "FFT" acquisition to obtain FRFs using a periodic chirp excitation, and then we choose an isolated natural frequency from the averaged FRF. After that we perform a "FAST SCAN" acquisition using a single-frequency excitation at the chosen frequency to obtain the corresponding ODS.

The noise level of the measured ODSs is primary determined by the frequency bandwidth B_w used in the "FAST SCAN" acquisition. The noise level is proportional to $\sqrt{B_w}$. However, the minimum bandwidth is limited to 0.02% of the excitation frequency, and the data acquisition time increases when B_w decreases.

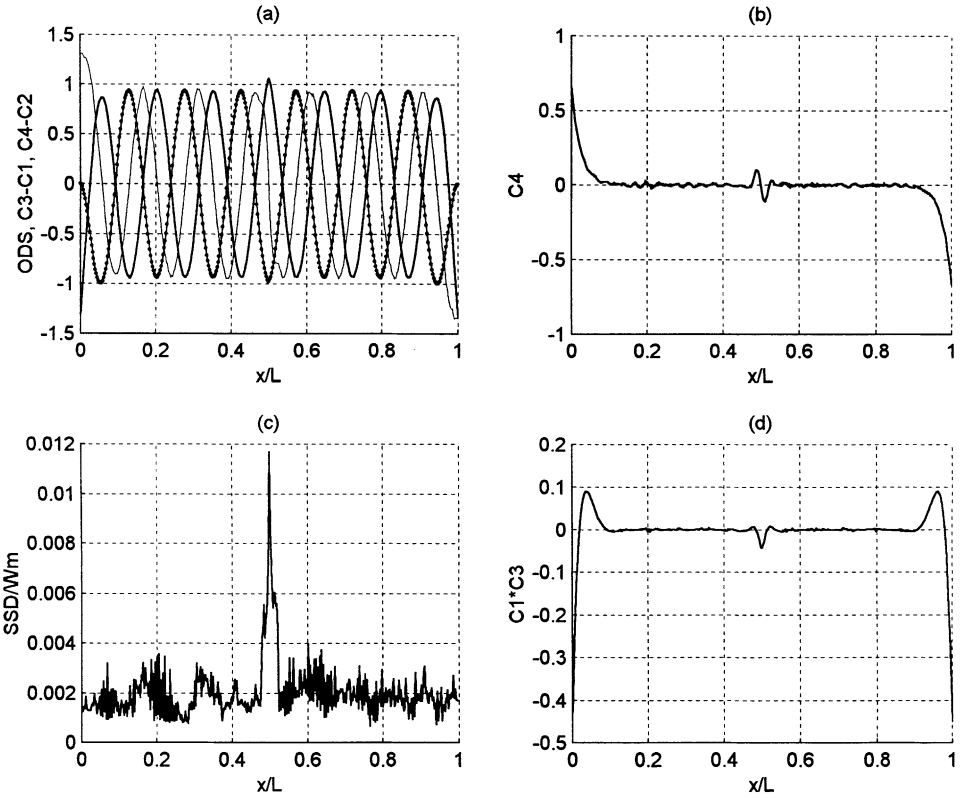

Fig. 12. Numerical damage locating curves when there is a center symmetric crack, $c = 0.055''$, $d = 0.15h$, 0.2% noise is added to the 13th mode shape, $N = 5$, and $\Delta = 2L/400$: (a) ODS, fitted ODS, $C_3 - C_1$, and $C_4 - C_2$, (b) C_4, (c) $\mathrm{SSD}/W_{\mathrm{m}}$, and (d) $C_1 * C_3$.

Hence, the noise level of high-frequency ODSs obtained using the "FAST SCAN" acquisition can be high. However, the noise level of the ODSs obtained in this study is estimated to have a standard deviation below 1% of the maximum value of the corresponding ODS.

4.2. Experimental results

Tests on six different structures with different types of damage are used here to show the reliability and robustness of the proposed BED method.

4.2.1. Case 1: a cantilevered beam with three cracks

Fig. 19 shows a $24.125'' \times 0.743'' \times 0.188''$ cantilevered aluminum beam with three cracks, which are actually narrow slots. The crack width is $0.055''$, and the crack depths are shown in the figure. Young's modulus is experimentally determined to be $E = 9.15 \times 10^6$ psi, and the mass density is $\rho = 5.2$ slug/ft^3. Cracks #2 and #3 are cut after Crack #1, and the crack depths of Cracks #1, #2, and #3 are about 28%, 16%, and 12% of the beam thickness, respectively. The laser beam from the laser vibrometer scans the backside of the beam to measure velocities of 200 or 400 equally spaced points.

Fig. 20 shows the results of processing the ODS corresponding to the sixth mode with only Crack #1. The unit of ODSs is meter/second, and W_{m} denotes the maximum value of the ODS. Crack #1 reduces the

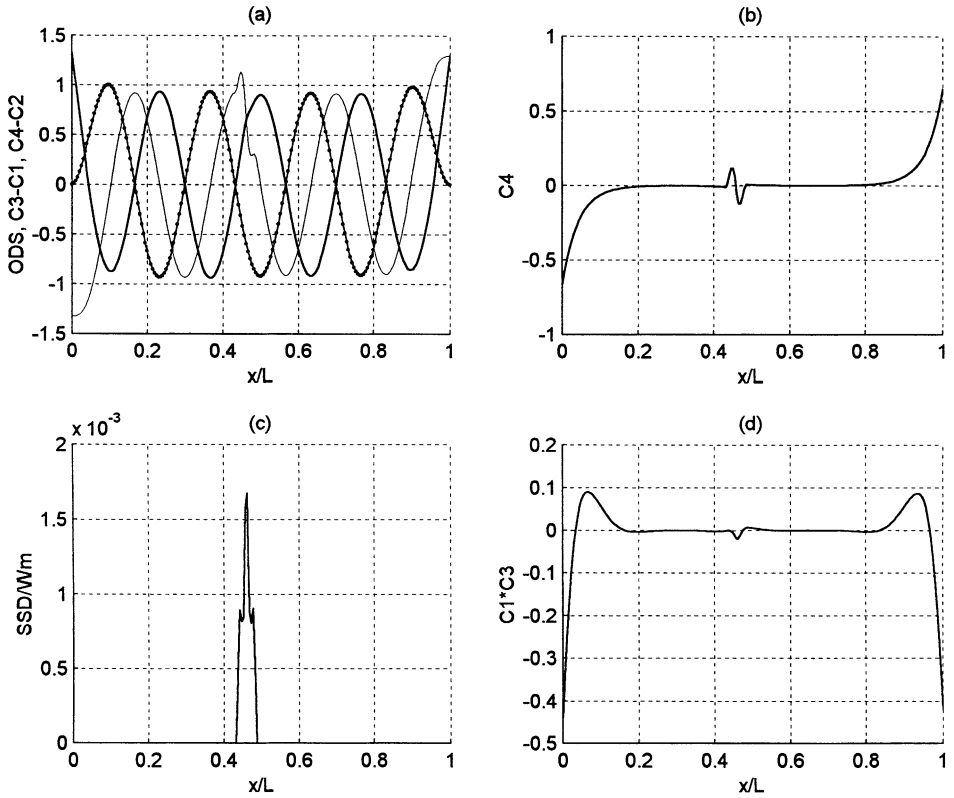

Fig. 13. Numerical damage locating curves when there is a symmetric crack with $c = 0.055''$ and $d = 0.15h$ at $x = 0.46L$: (a) ODS, fitted ODS, $C_3 - C_1$, and $C_4 - C_2$, (b) C_4, (c) SSD$/W_m$, and (d) $C_1 * C_3$.

6th natural frequency from 840.0 to 834.4 Hz according to the averaged FRF curve. Using the amplitude shown in Fig. 20(a) and the natural frequency one can show that the vibration amplitude is small and has a value of 0.025 mm. We use $N = 5$ and $\Delta x = 2L/200$ here, and the thin lines in Fig. 20(b)–(d) are obtained using $N = 5$ and $\Delta x = 4L/200$. We note that it is impossible to tell from Fig. 20(a) the difference between the measured ODS (dots) and the curve-fitted shape (the solid line connecting the dots) because the overall standard deviation SD is 0.13% of W_m. It is also impossible to find the crack location from the ODS.

Fig. 20(a) shows that, if a small Δx is used in the curve-fitting, the sudden changes on $C_3 - C_1$ and $C_4 - C_2$ show the possible areas of damage, but it is difficult to find the exact damage location because of noise. Moreover, when Δx increases, $C_3 - C_1$ and $C_4 - C_2$ smooth out quickly and it becomes impossible to find the crack from them. On the other hand, damage can be easily located using $C_1 * C_3$, C_4, and SSD.

Fig. 20(d) shows that, away from boundaries, $C_1 * C_3$ is zero except around the crack and it has a dimple at the exact crack location. Moreover, Fig. 20(b) shows that, away from boundaries, C_4 is zero except around the crack and it changes sign at the exact crack location. Furthermore, Fig. 20(c) shows that SSD has a peak at the crack location. To assure the identified locations of small cracks, one can check against each other the dimples on $C_3 * C_1$, the sign changes of C_4, and the peaks on SSD. Moreover, Fig. 20(b)–(d) shows that, when Δx increases, $C_3 - C_1$, $C_4 - C_2$, C_4, and $C_1 * C_3$ become smooth and SSD increases and peaks up at the crack location. Hence, overlapping damage locating curves obtained using two different window lengths makes damage locations more clear. The two peaks around $x/L = 0.2$ and 0.8 in Fig. 20(c)

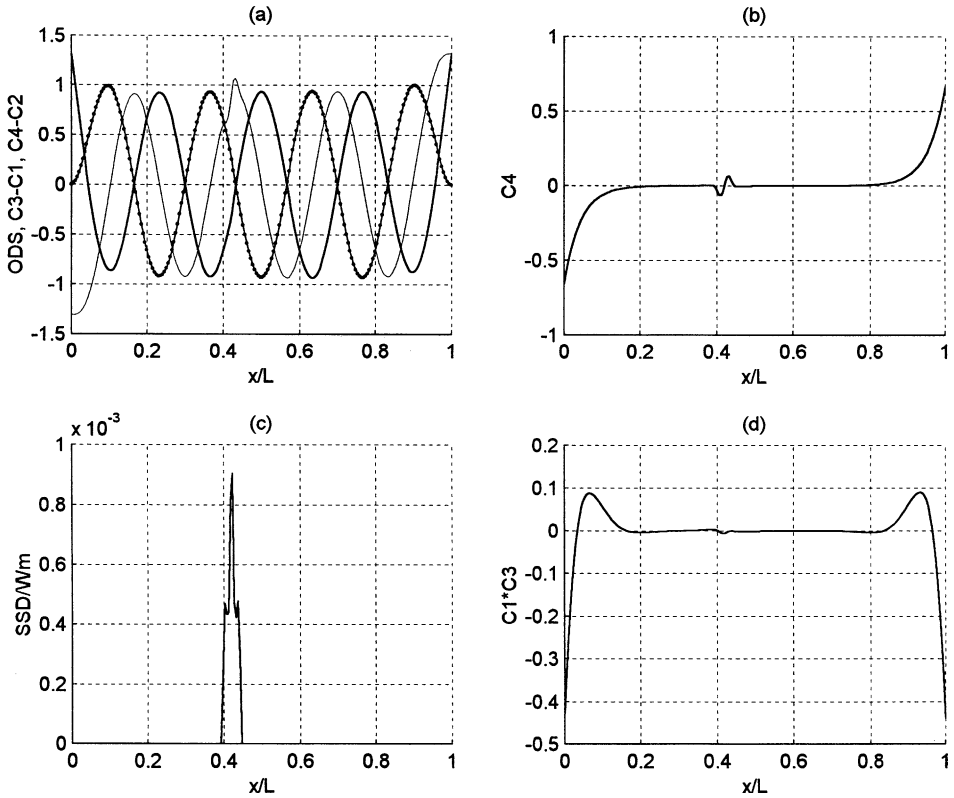

Fig. 14. Numerical damage locating curves when there is a symmetric crack with $c = 0.055''$ and $d = 0.15h$ at $x = 0.42L$: (a) ODS, fitted ODS, $C_3 - C_1$, and $C_4 - C_2$, (b) C_4, (c) SSD/W_m, and (d) $C_1 * C_3$.

do not increase when Δx increases, which indicates that they are not due to damage and are due to the laser vibrometer system itself or the surface condition of the beam.

Cracks #1–3 reduce the 8th natural frequency from 1551 to 1529 Hz according to the averaged FRF, where a frequency resolution of 0.781 Hz is used in the "FFT" acquisition. Fig. 21 shows the damage locating curves. Here, we use $N = 5$ and $\Delta x = 3L/400$, and the thin lines in Fig. 21(b)–(d) are obtained using $N = 5$ and $\Delta x = 5L/400$. Fig. 21(a) shows that it is difficult to locate the cracks using $C_3 - C_1$ and $C_4 - C_2$. However, one can easily identify the three crack locations from the dimples on $C_1 * C_3$, the sign changes of C_4, and the peaks on SSD. Because Crack #3 is smaller than the other two cracks and it is not right on one of the peaks of the ODS, the corresponding dimple on $C_1 * C_3$ is smaller. However, we point out here that a crack indicated by a small peak on SSD and a small dimple on $C_1 * C_3$ may not really be a small crack because it depends on the specific ODS under examination and the crack location.

Figs. 20(c) and 21(c) show that, when the window length increases, the SSD around $x = 0$ increases. This is because the actuation force from the PZT patch causes deviation of the ODS from the free vibration mode shape.

4.2.2. Case 2: a simply supported beam with five asymmetric side cracks

Fig. 22 shows a simply supported aluminum beam with five asymmetric side cracks. The crack width w of every crack is $0.045''$, and the crack depth d of each crack is shown in Fig. 22. Because of asymmetry, the

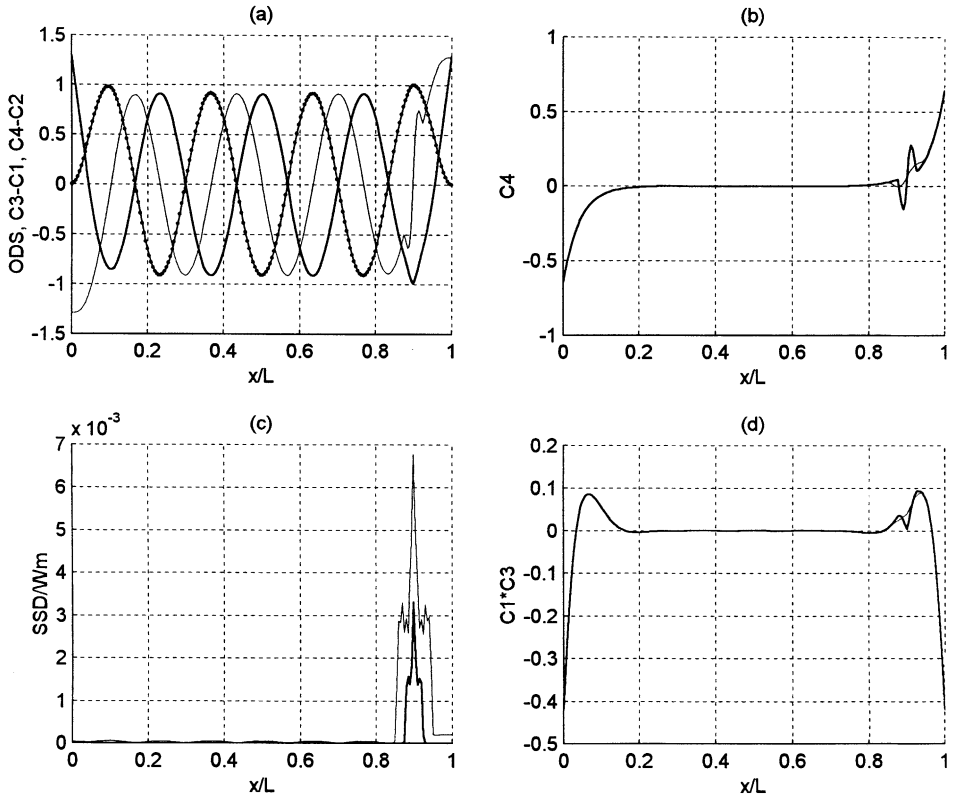

Fig. 15. Numerical damage locating curves when there is a symmetric crack with $c = 0.055''$ and $d = 0.15h$ at $x = 0.9L$: (a) ODS, fitted ODS, $C_3 - C_1$, and $C_4 - C_2$, (b) C_4, (c) SSD/W_m, and (d) $C_1 * C_3$.

beam vibration consists of transverse and torsional vibrations. This experiment is to test the robustness of the BED method in locating multiple cracks using a transverse ODS contaminated by torsional deformation.

We use $N = 5$ and $\Delta x = 3L/600$ in Fig. 23, and the thin lines in Fig. 23(b)–(d) are obtained using $\Delta x = 6L/600$. The frequency of the ODS is 3328 Hz. We note that the five cracks are clearly identified by the dimples on $C_1 * C_3$ and the peaks on SSD. Although C_4 is rough, it always changes sign at each crack location and the change is larger than those at other locations without damage. The dimple at Crack #1 in Fig. 23(d) is smaller than that at Crack #2 because Crack #1 is close to a node but Crack #2 is close to a peak of the ODS, as shown in Fig. 23(a).

The peak at the left side of Crack #1 on the thin line in Fig. 23(c) is caused by the excitation bending moment applied by the PZT patch.

4.2.3. Case 3: a clamped–clamped pretensioned beam with five side cracks

We find that it is difficult to use other lower-frequency ODSs of the beam shown in Fig. 22 to locate all cracks using only one ODS. Hence, we clamp the beam and apply an arbitrary pretension to the beam. The intention is to prevent torsional vibrations and to bring stress concentration effects into ODSs. The setup changes the left segment length in Fig. 22 to $5.95''$ and the right segment length to $6.33''$.

Fig. 24 shows that the five dimples on $C_1 * C_3$ and the five peaks on SSD clearly indicate the crack locations. We use $N = 5$ and $\Delta x = 3L/600$, and the thin curves in Fig. 24(b)–(d) are obtained using

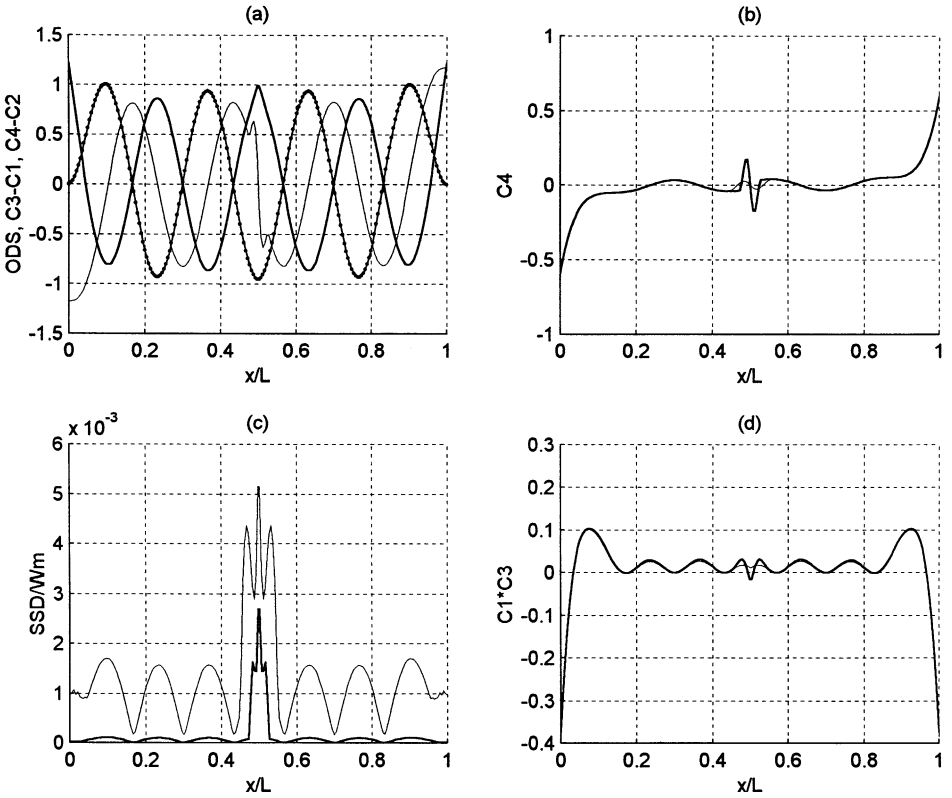

Fig. 16. Numerical damage locating curves when there is a center symmetric crack with $c = 0.055''$ and $d = 0.15h$ and the β is erroneously estimated: (a) ODS, fitted ODS, $C_3 - C_1$, and $C_4 - C_2$, (b) C_4, (c) SSD/W_m, and (d) $C_1 * C_3$.

$\Delta x = 6L/600$. The frequency of the ODS is 787.5 Hz, which is much lower than that of Fig. 23. Because of the use of a small Δx and a low-frequency ODS, $C_4 - C_2$ in Fig. 24(a) is rough.

4.2.4. Case 4: a cantilevered beam with four cracks and two holes

To further test the BED method we consider a $28.8'' \times 0.743'' \times 0.188''$ aluminum beam with four cracks and two holes through the beam width, as shown in Fig. 25. The crack width is $0.045''$, the crack depths d are shown in the figure, and the diameter D of holes is $0.086''$, which is about 46% of the beam thickness. Young's modulus is experimentally determined to be $E = 9.15 \times 10^6$ psi, and the mass density is $\rho = 5.2$ slug/ft^3.

We use $N = 5$ and $\Delta x = 2L/600$ in Fig. 26, and the thin lines in Fig. 26(b)–(d) are obtained using $\Delta x = 6L/600$, where the frequency of the ODS is 1637 Hz. We note that all the four cracks are clearly indicated by the dimples on $C_1 * C_3$ and the peaks on SSD. Fig. 26(d) shows that, although Crack #6 is within a boundary-layer zone, this method still can locate it. To identify cracks within boundary layers, one needs to subtract the curve obtained using a large Δx from the curve obtained using a small Δx.

The two holes cannot be identified in Fig. 26 because each of them is close to a node of the ODS. Hence, we use another ODS to locate them, as shown in Fig. 27. We use $N = 5$ and $\Delta x = 2L/600$ in Fig. 27, and the thin lines in Fig. 27(b)–(d) are obtained using $\Delta x = 6L/600$, where the frequency of the ODS is 2015 Hz. We note that all the four cracks and two holes are clearly indicated by the dimples on $C_1 * C_3$. However,

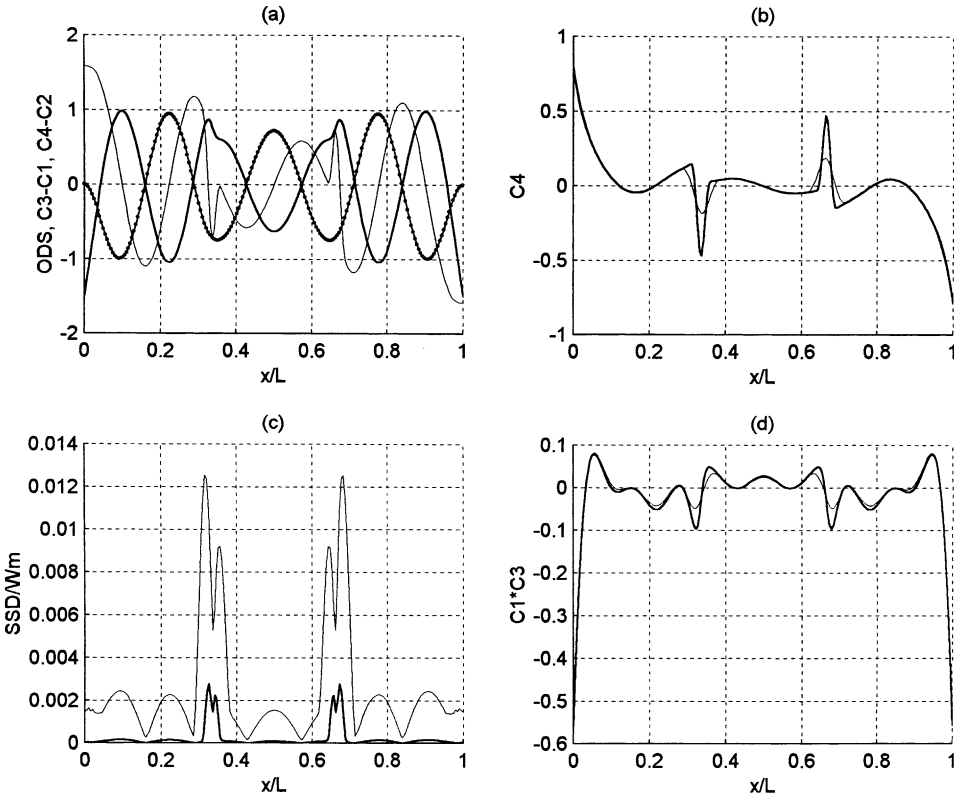

Fig. 17. Numerical damage locating curves when the thickness of the segment between $x = 0.5L - 4''$ and $x = 0.5L + 4''$ is $1.3h$: (a) ODS, fitted ODS, $C_3 - C_1$, and $C_4 - C_2$, (b) C_4, (c) SSD/W_m, and (d) $C_1 * C_3$.

because Cracks #1 and #3 are not at the peaks of this ODS, the dimples are smaller than those in Fig. 26(d). Moreover, because the two holes are not at the peaks of the ODS and because these holes are in low-stress areas and do not significantly reduce the bending stiffness, the two corresponding dimples on $C_1 * C_3$ are also small and the holes are not clearly shown on the SSD curve. This observation reveals that it may be better to use longitudinal or torsional ODSs, instead of bending ODSs, for detecting internal holes. This topic requires more studies.

4.2.5. Case 5: a rectangular plate with one hole

Fig. 28 shows a $30'' \times 22.8'' \times 0.122''$ aluminum plate with a hole through its thickness. The diameter of the hole is $0.162''$, which is a little bit larger than the plate thickness. The plate is slightly curved. Vibration velocities of points along two lines equally separated by the hole at the mid point by $0.7''$ are obtained. The ODS along the line passing through the hole is estimated by taking the average of the two ODSs measured along the two lines. Fig. 29 shows the obtained damage locating curves. We use $N = 5$ and $\Delta x = 2L/477$, and the thin lines in Fig. 29(b) and (d) are obtained using $\Delta x = 6L/477$. The ODS is a low-order one, and the frequency is 1717 Hz. This low-order ODS is chosen because the $2'' \times 1'' \times 0.015''$ PZT patch attached at the center of the backside of the plate is too small to excite other high-order ODSs to have enough amplitudes. The thin line in Fig. 29(d) is not zero at points away from the boundaries because this ODS has a non-zero Gaussian curvature (Shames and Dym, 1985). Subtracting the thin line from the thick curve in Fig. 29(d) yields a curve that has a big dimple around $x = 0.5L$ with a shape similar to that in Fig. 20(d)

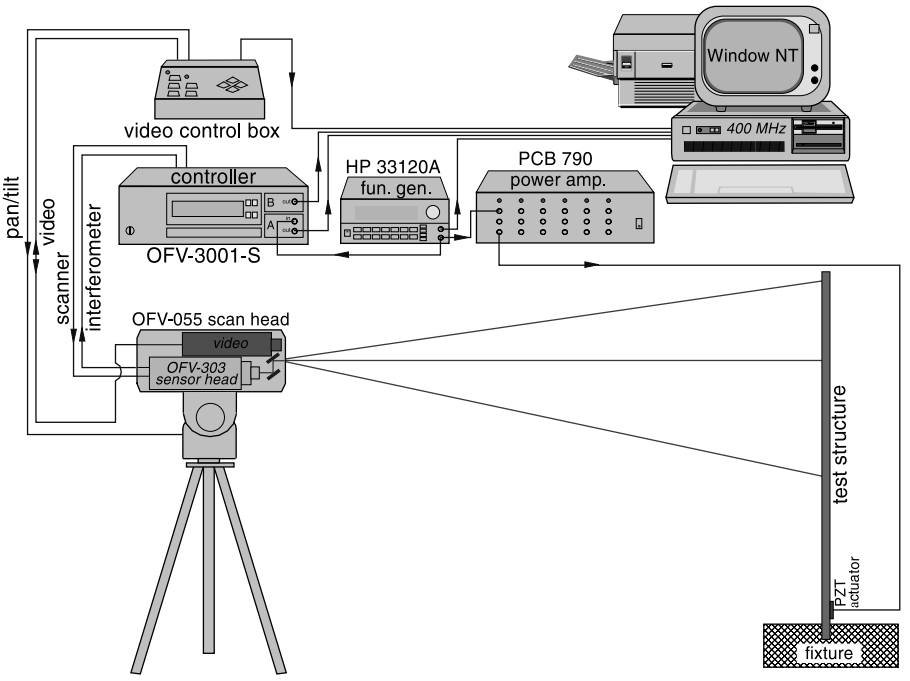

Fig. 18. The experimental setup for measuring operational deflection shapes of structures using a PSV-200 scanning laser vibrometer and a PZT patch.

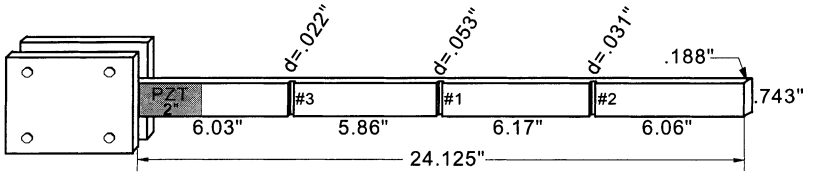

Fig. 19. A cantilevered aluminum beam with three cracks.

around Crack #1, which assures that it is a damage location. On the other hand, the dimple around $x/L = 0.34$ is due to measurement noise because its shape is different from that of a damage. The peak on SSD and the sign change of C_4 also confirm the damage location.

4.2.6. Case 6: a cantilevered thick beam with an actual crack

Fig. 30 shows a $14.5'' \times 1.8'' \times 0.5''$ aluminum beam with an actual through-the-thickness side crack at the mid point of the scanned length. The crack depth is unknown but is estimated to be about $0.3b = 0.54''$. It is difficult to detect the crack using naked eyes, and it is hard to open the crack because the beam is thick. However, the damage curves obtained using the ODS at 3060 Hz clearly show the location of the crack, as shown in Fig. 31. We use $N = 5$ and $\Delta x = 2L/200$ in Fig. 31, and the thin lines in Fig. 31(b) and (d) are obtained using $\Delta x = 6L/200$. Using the amplitude shown in Fig. 31(a) and the natural frequency one can show that the vibration amplitude is very small and has a value of 2.6 μm. We point out here that the ODS is a low-order one because it is difficult to excite high-order ODSs of this thick beam to have certain amplitude values by using a small PZT patch.

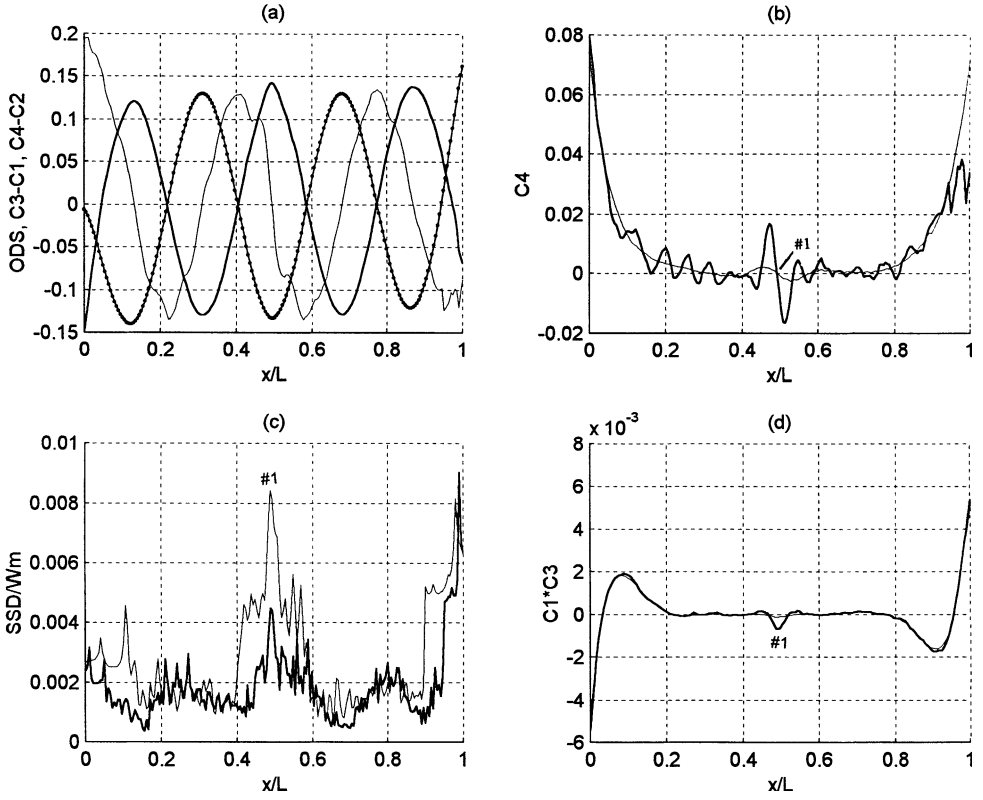

Fig. 20. Experimental damage locating curves of the beam in Fig. 19 with Crack #1: (a) ODS (dots), fitted ODS (solid line connecting dots), $C_3 - C_1$ (thick line), and $C_4 - C_2$ (thin line), (b) C_4, (c) SSD/W_m, and (d) $C_1 * C_3$.

4.3. Discussion

The BED method works because boundary-layer solutions can be separated from central solutions by using the proposed sliding-window curve-fitting method and because each C_i in Eq. (5) has a physical meaning. Moreover, results show that each C_i requires a different sliding-window length in order to smooth its curve. Hence, damage locating curves obtained using two different sliding-window lengths can be overlapped to reveal damage. The BED method also provides multiple damage indicators. $C_1 * C_3$ indicates crack locations by dimples, SSD indicates crack locations by peaks, and C_4 indicates crack locations by sign changes. Results show that SSD has the highest sensitivity to damage and measurement noise, and $C_1 * C_3$ has the lowest sensitivity.

The merits of the BED method are summarized here.

(1) This is a model-independent method; no model is required for comparison.

(2) Setting-up a scanning laser vibrometer for on-site vibration measurements requires much less time than setting-up a conventional multiple-sensor system, and this method can examine large structural systems easily and quickly.

(3) Because this method only requires the excitation force to be periodic, it can be used for on-site damage inspection using working excitations, such as excitations caused by the operating engine of the vehicle under examination.

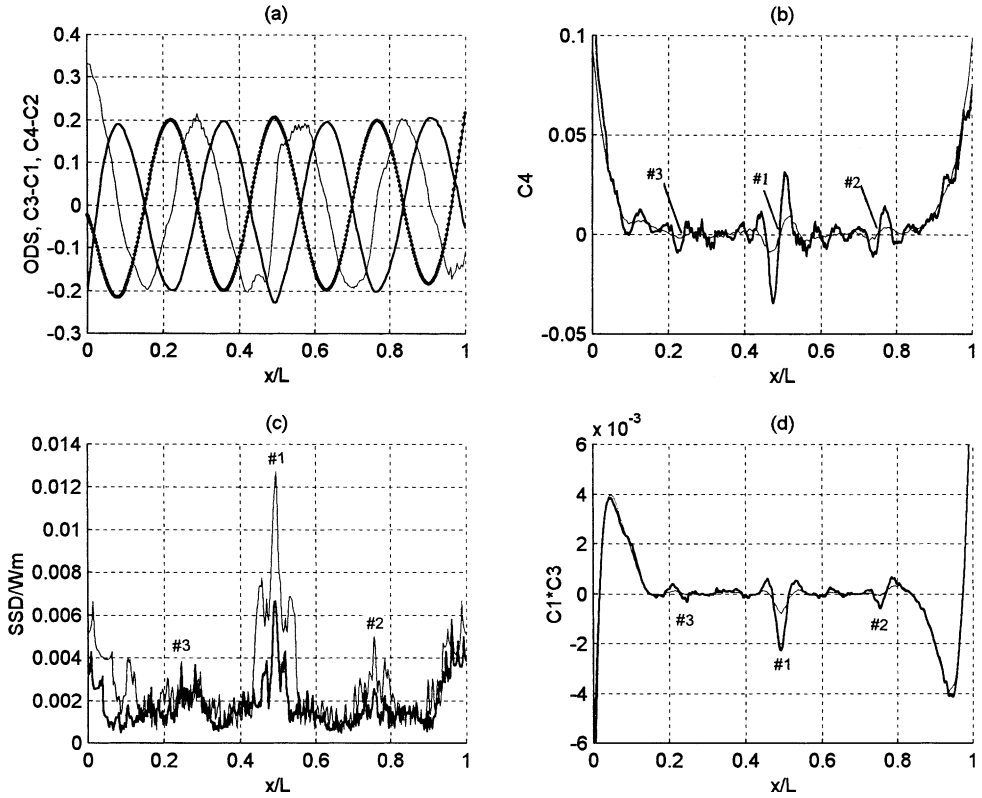

Fig. 21. Experimental damage locating curves of the beam in Fig. 19 with the three cracks: (a) ODS, fitted ODS, $C_3 - C_1$, and $C_4 - C_2$, (b) C_4, (c) SSD/W_m, and (d) $C_1 * C_3$.

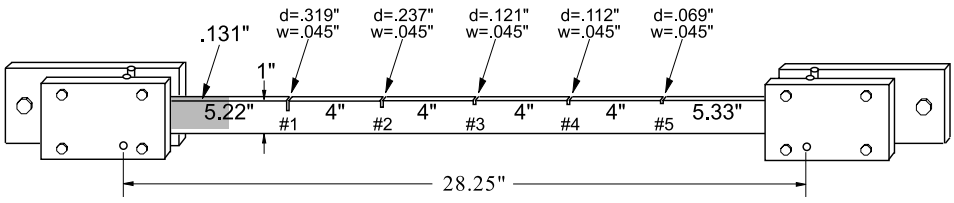

Fig. 22. A simply supported aluminum beam with five side slots.

(4) Because this method uses no historical data, it works even when the dynamic characteristics of a structure are changed by harmless environmental factors, such as temperature, moisture, and boundary conditions.

(5) This method provides multiple damage indicators that can be used to check against each other to ensure the identified damage locations.

(6) Because this method uses only experimental ODSs, identified damage locations can be easily pointed out by using the visual and laser pointing system of the Polytec PSV-200 scanning laser vibrometer.

(7) This method can provide different levels of accuracy for different levels of inspection and maintenance. For a low-level inspection, only a small number of points need to be measured.

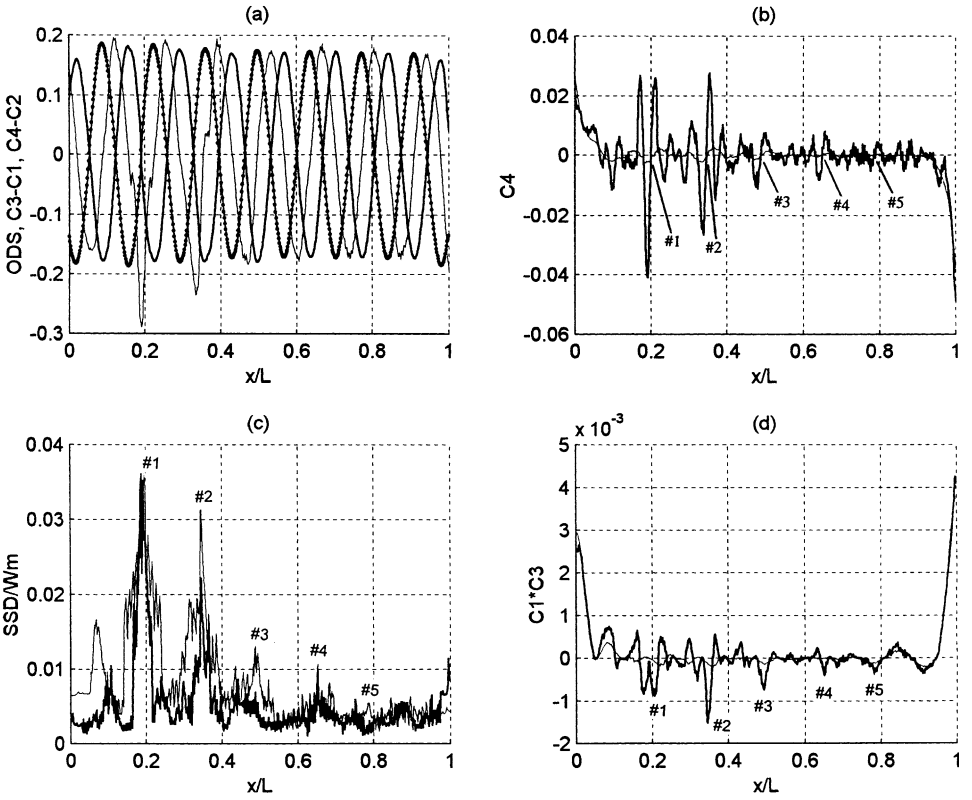

Fig. 23. Experimental damage locating curves of the beam in Fig. 22: (a) ODS, fitted ODS, $C_3 - C_1$, and $C_4 - C_2$, (b) C_4, (c) SSD/W_m, and (d) $C_1 * C_3$.

The experimental results show that the BED method can detect small surface cracks having a crack depth of 12% of the beam thickness and small side cracks having a crack depth of 7% of the beam width. To improve the sensitivity and accuracy of this BED method and to develop it into a method for actual on-site structural damage detection the following problems require more studies.

(1) One ODS can only detect damage around its peaks. To ensure all possible damages will be located, several ODSs with their peaks covered the whole structural area need to be examined. Choosing the appropriate ODSs is a problem to be solved.

(2) The noise level of the measured ODSs is primary determined by the frequency bandwidth B_w used in the "FAST SCAN" acquisition. The noise level is proportional to $\sqrt{B_w}$. Hence, one can reduce $\sqrt{B_w}$ to reduce noise. However, the minimum bandwidth is 0.02% of the excitation frequency, and the data acquisition time increases when B_w decreases. Hence, the noise level of a high-frequency ODS obtained using the "FAST SCAN" acquisition can be high, and the acquisition time can be long. Hence, how to reduce the frequency bandwidth needs to be studied.

(3) The accuracy of this method is controlled by the measurement noise contained in ODSs. Hence, the noise pattern of ODSs needs to be studied.

(4) Because of measurement noise, the ODS amplitude needs to have a certain value in order to contain clear information of small cracks. Moreover, the results show that high-frequency ODSs are better than low-frequency ODSs for locating damage. However, a high-frequency ODS requires high power in order to have a significant amplitude. Hence, a high-power amplifier is needed.

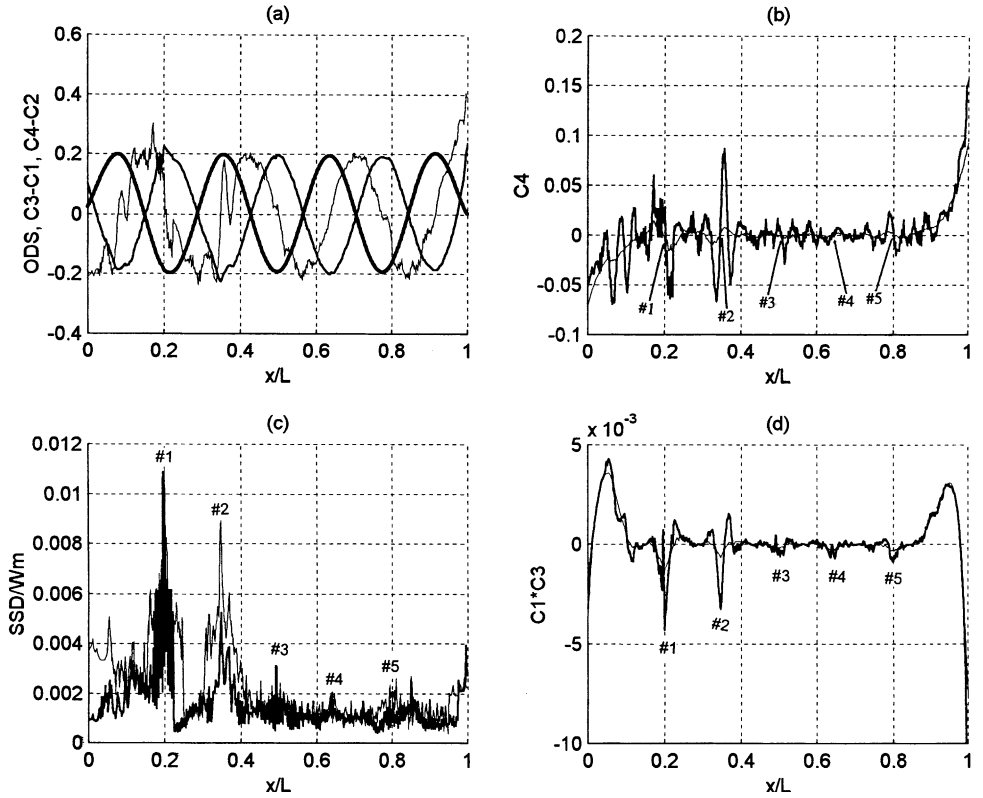

Fig. 24. Experimental damage locating curves of the beam in Fig. 22 with both ends clamped: (a) ODS, fitted ODS, $C_3 - C_1$, and $C_4 - C_2$, (b) C_4, (c) SSD/W_m, and (d) $C_1 * C_3$.

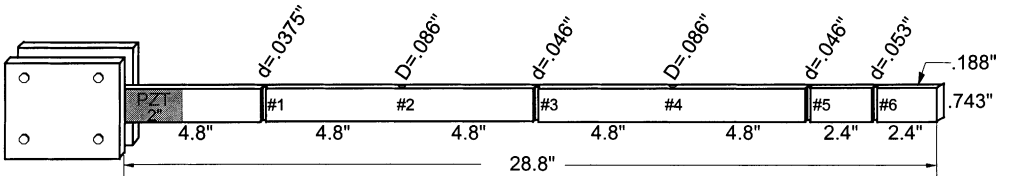

Fig. 25. A cantilevered aluminum beam with four cracks and two internal holes.

(5) For very thick and stiff structures, only low-order ODSs can be excited. Because low-order ODSs have small W'' and W'''' and their boundary-layer solutions spread across the whole structure, it is difficult to find cracks using low-order ODSs. Modification of the BED method for detecting damage using low-order ODSs needs to be studied.

(6) If the measured area is of nonuniform thickness or material, boundary effects exist everywhere. Extraction of the boundary effects due to damage from the boundary solutions needs more studies.

(7) The experimental results shown in Fig. 29 indicate that the BED method also works for structures with small initial curvatures. To work for shell-type structures with significant initial curvatures the BED method needs to be modified.

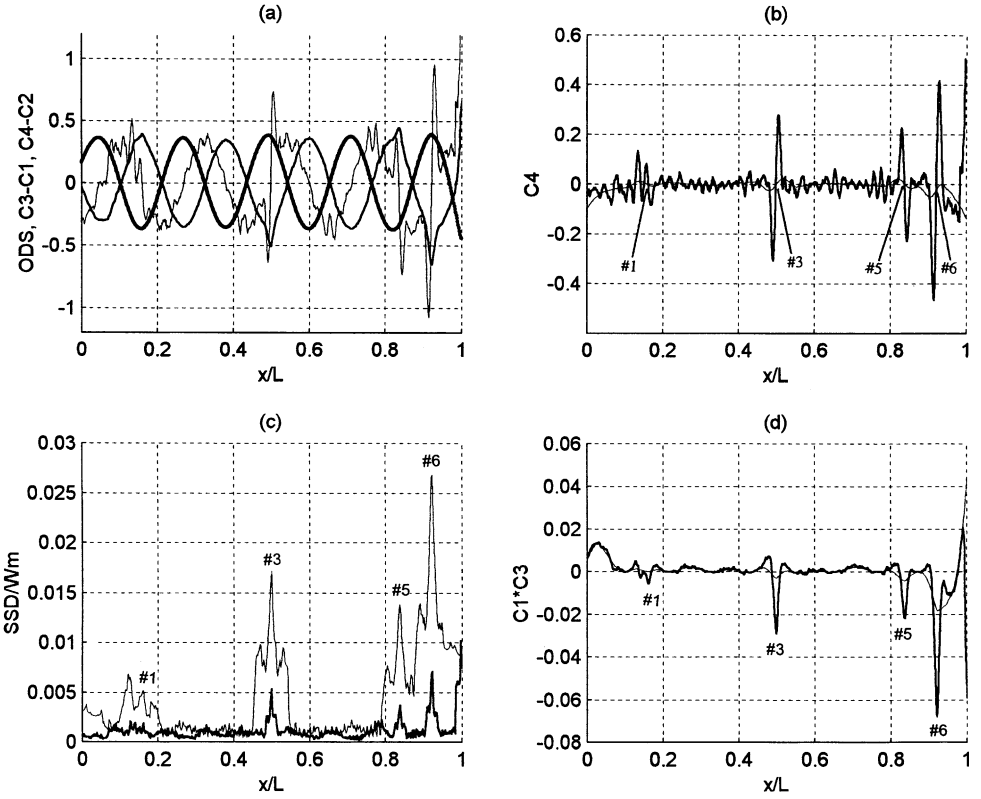

Fig. 26. Experimental damage locating curves of the beam in Fig. 25 when a 1637-Hz ODS is used: (a) ODS, fitted ODS, $C_3 - C_1$, and $C_4 - C_2$, (b) C_4, (c) SSD/W_m, and (d) $C_1 * C_3$.

(8) Torsional and longitudinal ODSs are shown in Sections 2.2 and 2.3 to be appropriate for using the BED method to locate damage, but it is difficult to excite such ODSs using PZT patches, even using the concept of bi-moments (Pai et al., 1997). Moreover, although one can assume $\beta_1 = \beta$ in Eqs. (20) and (23) when using the BED method, the obtained boundary-layer solutions change when the sliding-window length changes.

5. Concluding remarks

The BED method works by extracting boundary-layer solutions from experimental ODSs using a sliding-window least-squares curve-fitting method. Boundary-layer solutions are sensitive to damage, and they provide multiple damage indicators that can be checked against each other to assure the identified damage locations. The BED method requires no model or historical data for comparison. Numerical simulations are performed to show the BED method in locating different types of damage. Experiments are performed on several different beams with different types of damages. Numerical and experimental results show that the BED method is sensitive and reliable for locating small damages. However, more studies are needed before this method can be used for on-site structural damage detection.

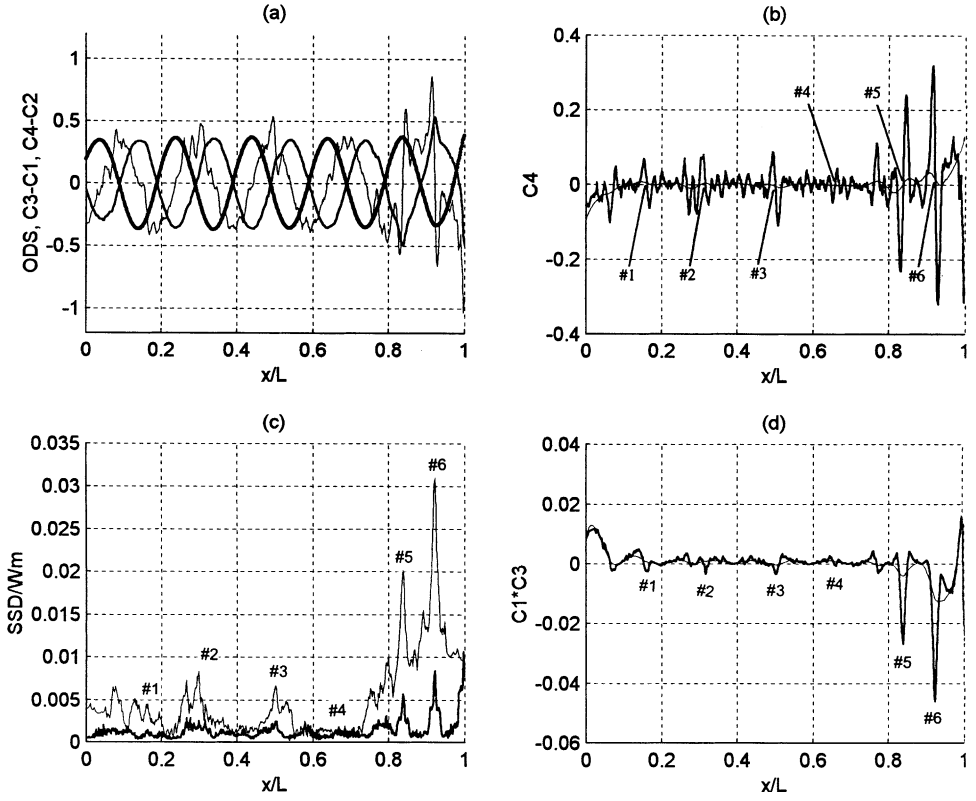

Fig. 27. Experimental damage locating curves of the beam in Fig. 25 when a 2015-Hz ODS is used: (a) ODS, fitted ODS, $C_3 - C_1$, and $C_4 - C_2$, (b) C_4, (c) SSD/W_m, and (d) $C_1 * C_3$.

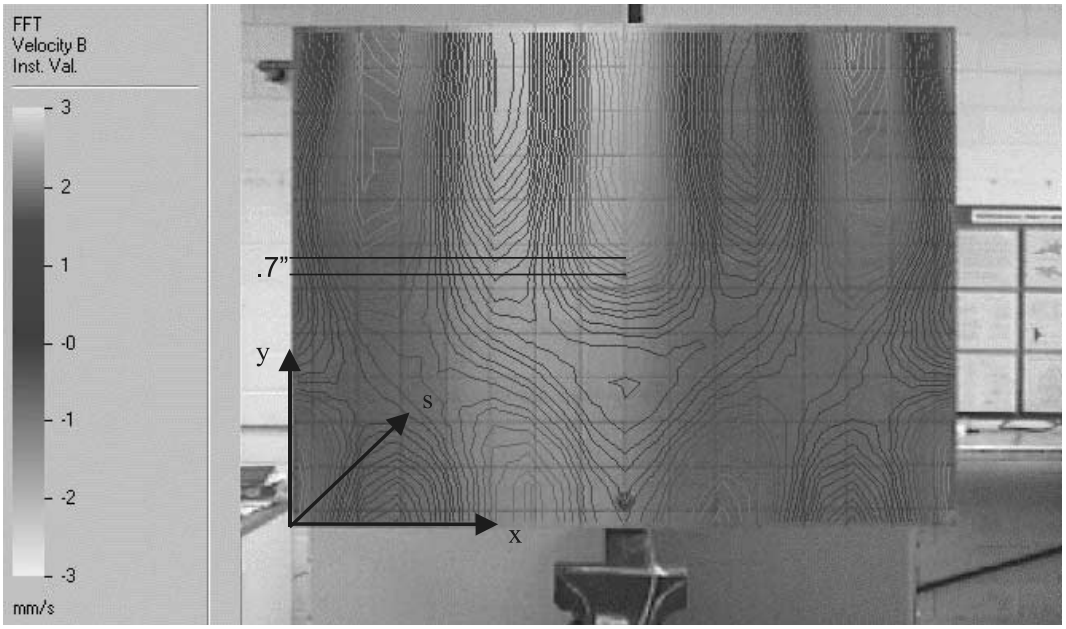

Fig. 28. A 30″ × 22.8″ × 0.122″ aluminum plate with a hole having a diameter of 0.162″.

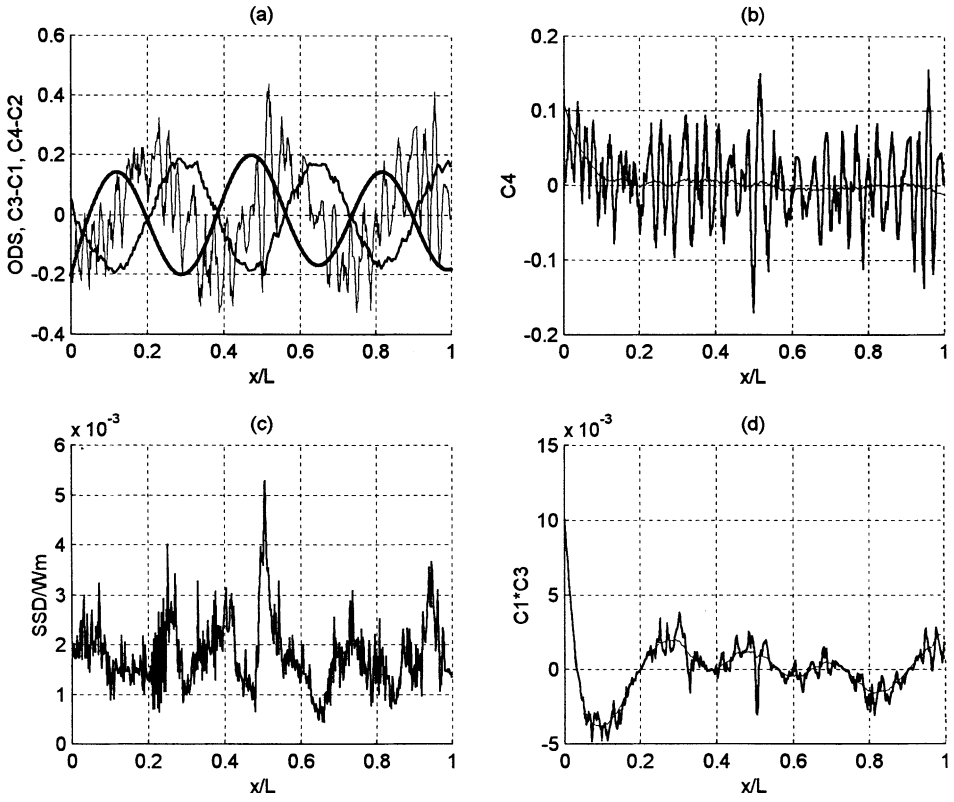

Fig. 29. Experimental damage locating curves of the plate in Fig. 28: (a) ODS, fitted ODS, $C_3 - C_1$, and $C_4 - C_2$, (b) C_4, (c) SSD/W_m, and (d) $C_1 * C_3$.

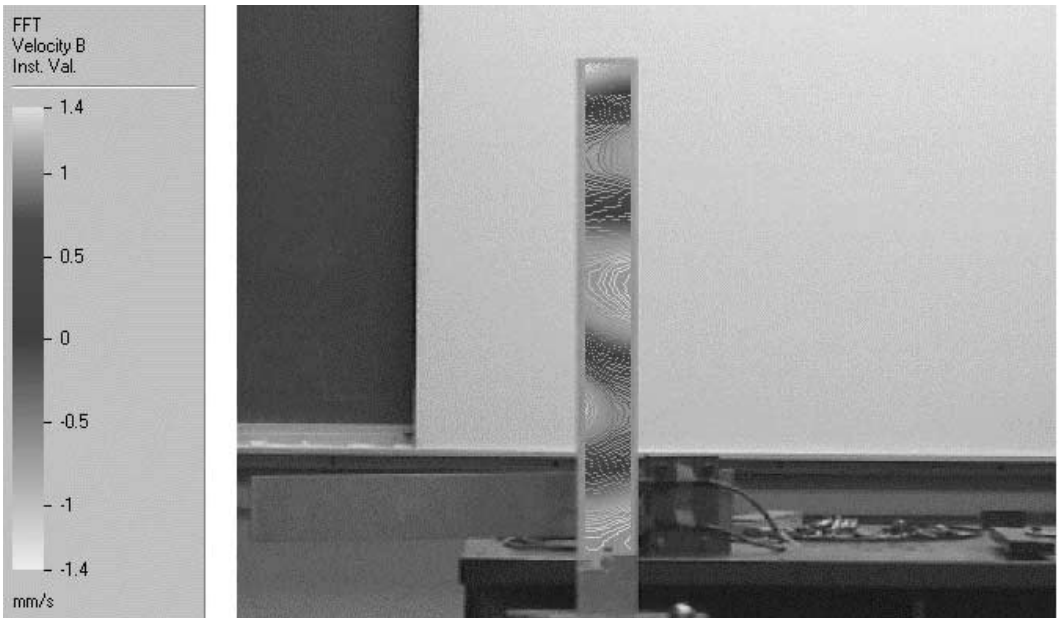

Fig. 30. A 14.5″ × 1.8″ × 0.5″ cantilevered aluminum beam with an actual through-the-thickness side crack at the mid point of the scanned length.

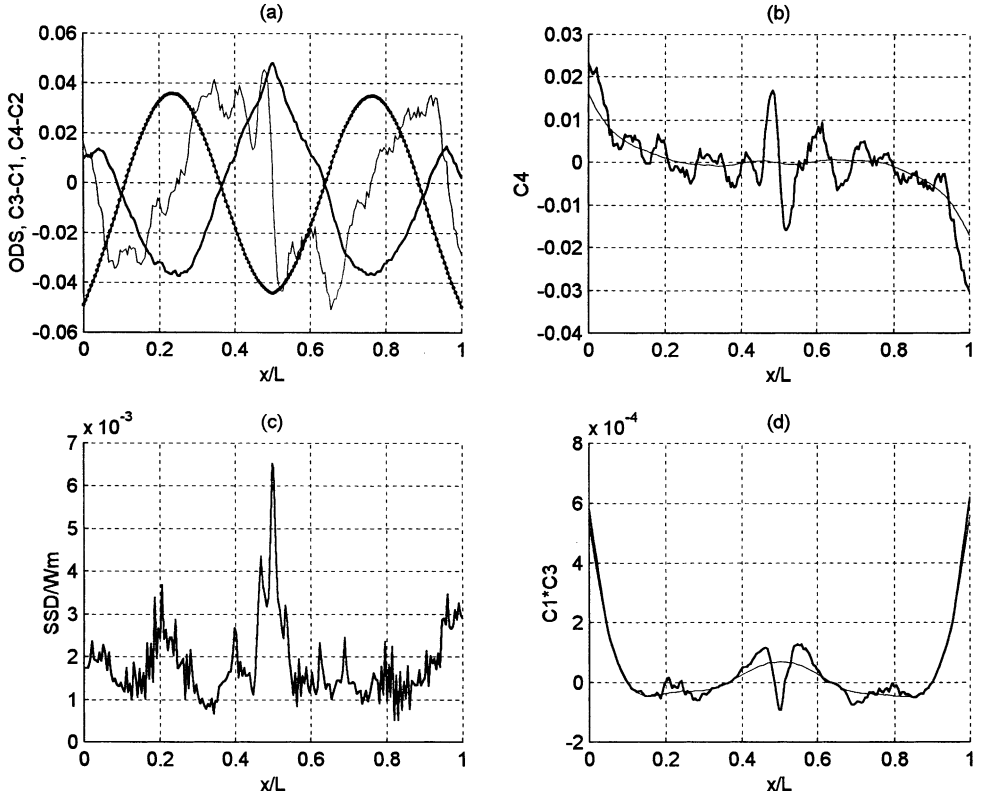

Fig. 31. Experimental damage locating curves of the beam in Fig. 30: (a) ODS, fitted ODS, $C_3 - C_1$, and $C_4 - C_2$, (b) C_4, (c) SSD/W_m, and (d) $C_1 * C_3$.

Acknowledgements

This work is supported by the National Science Foundation through Grant CMS-9871288. Dr. Shih-Chi Liu is the technical monitor. The support is gratefully acknowledged.

References

Doebling, S.W., Farrar, C.R., Prime, M.B., Shevitz, D.W., 1996. Damage identification and health monitoring of structural and mechanical systems from changes in their vibration characteristics: A literature review, Report No. LA-13070-MS, Los Alamos National Laboratory.

Dugundji, J., 1988. Simple expressions for higher vibration modes of uniform Euler beams. AIAA Journal 26 (8), 1013–1014.

Giavotto, V., Borri, M., Mantegazza, P., Ghiringhelli, G., Carmaschi, V., Maffioli, G.C., Mussi, F., 1983. Anisotropic beam theory and applications. Computers and Structures 16, 403–413.

Iesan, D., 1987. St. Venant's Problem, Lecture Notes in Mathematics, No. 1279, In: Dold, A., Eckmann, B. (Eds.), Springer, New York.

Kam, T.Y., Lee, T.Y., 1994. Identification of crack size via an energy approach. Journal of Nondestructive Evaluation 13, 1–11.

Pai, P.F., Jin, S., 2000. Locating structural damage by detecting boundary effects. Journal of Sound and Vibration 231 (4), 1079–1110.

Pai, P.F., Wen, B., Naser, A.S., Schulz, M.J., 1997. Nonlinear vibration suppression of cantilever beams using bi-moment induced by PZT actuators. 38th Structures, Structural Dynamics, and Materials Conference, Hyatt Orlando, Kissimmee, Florida, April 7–10.

Shames, I.H., Dym, C.L., 1985. Energy and Finite Element Methods in Structural Mechanics. McGraw-Hill, New York.
Shen, M.H.H., Pierre, C., 1990. Natural modes of Bernoulli-Euler beams with symmetric cracks. Journal of Sound and Vibration 138 (1), 115–134.
Sirohi, R.S., Tay, C.J., Shang, H.M., Boo, W.P., 1999. Nondestructive assessment of thinning of plates using digital shearography. Optical Engineering 38 (9), 1582–1585.
Vlasov, V.Z., 1961. Thin-Walled Elastic Beams, Israel Program for Scientific Translations Ltd, Jerusalem.